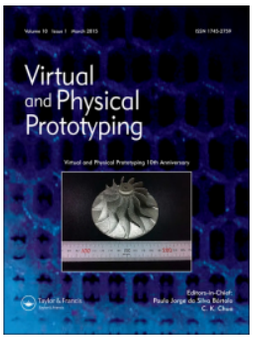

Virtual and Physical Prototyping

ISSN: (Print) (Online) Journal homepage: www.tandfonline.com/journals/nvpp20

Machine learning-based prediction and optimisation framework for as-extruded cell viability in extrusion-based 3D bioprinting

Colin Zhang, Kelum Chamara Manoj Lakmal Elvitigala, Wildan Mubarok, Yasunori Okano & Shinji Sakai

To cite this article: Colin Zhang, Kelum Chamara Manoj Lakmal Elvitigala, Wildan Mubarok, Yasunori Okano & Shinji Sakai (2024) Machine learning-based prediction and optimisation framework for as-extruded cell viability in extrusion-based 3D bioprinting, Virtual and Physical Prototyping, 19:1, e2400330, DOI: 10.1080/17452759.2024.2400330

To link to this article: https://doi.org/10.1080/17452759.2024.2400330

Published online: 11 Sep 2024.

VIRTUAL AND PHYSICAL PROTOTYPING
2024, VOL. 19, NO. 1, e2400330 (25 pages)
https://doi.org/10.1080/17452759.2024.2400330

Taylor & Francis
Taylor & Francis Group

Machine learning-based prediction and optimisation framework for as-extruded cell viability in extrusion-based 3D bioprinting

Colin Zhang, Kelum Chamara Manoj Lakmal Elvitigala, Wildan Mubarok, Yasunori Okano and Shinji Sakai

Division of Chemical Engineering, Department of Materials Engineering Science, Graduate School of Engineering Science, Osaka University, Toyonaka, Japan

ABSTRACT

Extrusion-based 3D bioprinting has revolutionised tissue engineering, enabling complex biostructure manufacturing. However, extrusion imposes substantial shear stress on cells, compromising cell viability. Predicting and optimising cell viability remains challenging due to rheological modelling complexity and cell-type dependency. To address these challenges, this study developed a quantitative framework integrating numerical simulation and machine learning. Support vector regression and simulation were utilised to evaluate alginate ink viscosity and shear stress profiles, while multi-layer perceptron regressors were trained on experimental datasets for diverse cell types to predict as-extruded cell viability based on wall shear stress magnitude and exposure time. Results showed vascular endothelial cells were most susceptible to shear stress, with viability dropping to 80% at 2.05 kPa for 400 ms, while mesenchymal stem, cervical cancer, and embryonic fibroblast cells showed such decrease at 2.65, 2.85, and 3.72 kPa, respectively. This versatile framework enables rapid bioink optimisation across various cell types.

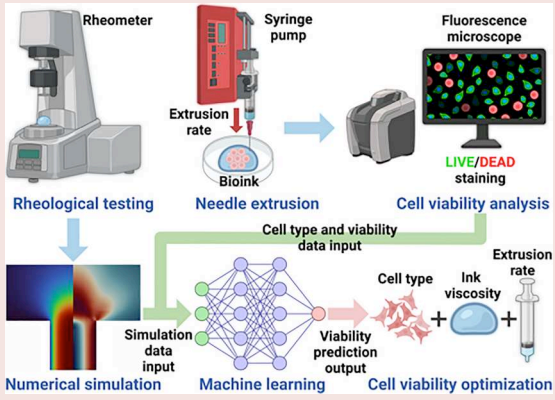

ARTICLE HISTORY
Received 12 June 2024
Accepted 29 August 2024

KEYWORDS
3D bioprinting; cell viability; shear stress; numerical analysis; machine learning; alginate-based bioink

Highlights

- A quantitative framework integrates advanced rheological modelling, CFD simulations, and machine learning to predict and optimise as-extruded cell viability in extrusion-based 3D bioprinting.
- High-accuracy predictive machine learning models for ink rheology and as-extruded cell viability across multiple cell types.
- A robust and generalisable approach that can rapidly adapt to various bioinks and cell types, accelerating bioink optimisation.
- Experimental validation confirms the framework's effectiveness and applicability in achieving optimal as-extruded cell viability.

1. Introduction

Three-dimensional (3D) bioprinting is a transformative technology in tissue engineering and regenerative medicines that utilises additive manufacturing techniques to produce complex and heterogeneous biostructures [1,2]. Bioink, a printable cell-containing biomaterial, is the building material in the printing

CONTACT Shinji Sakai sakai@cheng.es.osaka-u.ac.jp Division of Chemical Engineering, Department of Materials Engineering Science, Graduate School of Engineering Science, Osaka University, 1-3 Machikaneyama-cho, Toyonaka, Osaka, 560-8531, Japan

process [3]. The most commonly available 3D bioprinting methods include extrusion-based, inkjet-based, laser-assisted, and stereolithography-based bioprinting [4]. Compared with other bioprinting strategies, the main advantages of extrusion-based 3D bioprinting include cost-effectiveness, ease of operation, disposition of high cell density, and the ability to print with a wide range of viscosities, including high viscosity inks, which can improve printability [5–7]. Besides typical direct extrusion (self-support) bioprinting, the versatility has led to the development of various extrusion bioprinting techniques [8]. These include bath-support and coaxial extrusion, which involve printing bioinks into a supportive bath or simultaneously extruding multiple bioinks through concentric nozzles, respectively, with both methods being influenced by shear stress that affects cell viability during the extrusion process [8–10].

Most bioinks employed in extrusion-based 3D bioprinting are non-Newtonian fluids and exhibit shear-thinning properties, where the apparent viscosity of the bioink decreases as the applied shear rate increases [11,12]. Alginate-based bioinks are especially prevalent in extrusion-based 3D bioprinting due to their pronounced shear-thinning properties, high biocompatibility, and resemblance to the extracellular matrix (ECM) [13,14]. The shear-thinning property is beneficial as it can minimise the chances of clogging and enhance cell viability during the extrusion process [15,16]. However, the magnitude of shear stress can still be significant for higher extrusion rates and polymer concentrations, leading to a substantial reduction in cell viability [17,18].

Shear stress is the primary cause of cell damage during the extrusion-based 3D bioprinting process [19–21]. Previous studies indicate that exposure to a high magnitude of shear stress, even in the short term, can negatively impact cell viability [22,23]; however, further research is needed to elucidate and quantify the relationship between applied shear stress and resulting cell damage and determine the range of shear stress that maintains cell integrity [24]. Several strategies have been proposed to address the challenges. For instance, utilising needles with larger inner diameters can reduce extrusion pressure and shear stress, although this compromises the printing resolution [25]. Other research also points out that tapered nozzles can enhance cell viability by minimising the exposure time in high-shear stress regions [16]. However, cylindrical needles have been shown to improve shape fidelity and stacking accuracy when printing scaffold structures [26]. Cylindrical needles are also essential for the free-form reversible embedding of suspended hydrogels (FRESH) method since they can minimise the disturbance inside the supporting solutions or viscous materials [27]. Building on this approach, Li et al. explored a hydrogel pair suitable for both the non-submerged and submerged 3D printing approaches, demonstrating the adaptability of extrusion-based 3D bioprinting techniques [28]. Another resolution is to decrease the concentration of the polymer ink, which reduces the overall ink's apparent viscosity and, hence, the magnitude of shear stress [29]. However, this can slow down the crosslinking reaction rate and make the ink more prone to spreading due to reduced rheological stability and printability, causing the printed structure to collapse [30]. These challenges highlight the need for a comprehensive approach to predict and optimise printability and cell viability. Addressing this need, Li et al. proposed a rheological method to estimate 3D printability by calculating shear rates on cells during extrusion [31]. While this method offers assessments of printability, a framework for predicting and optimising cell viability is still necessary for successful extrusion-based 3D bioprinting.

The experimental study of cell viability in extrusion-based 3D bioprinting has mainly focused on limited cell lines and lacks generalizability. Ouyang et al. investigated the cell viability of embryonic stem cells under varying ink concentrations, printing temperatures, and holding time, highlighting the detrimental effect of wall shear stress on cell viability, though exposure time to such shear stress was not studied [32]. Meanwhile, computational fluid dynamics (CFD) simulation provides a straightforward way to characterise the shear stress profile inside the printhead. Previous studies examined the shear stress distribution for various needle geometries and dimensions, such as cylindrical needles, tapered nozzles, and customised printheads [17,33,34]. However, these studies often rely on cell viability data from other literature sources, limiting their ability to directly correlate shear stress and exposure time with experimental cell viability outcomes; in this study, multiple cell lines from diverse tissue origins and functionalities were directly compared at the same time, ensuring consistency and accuracy. Moreover, CFD simulation approaches to evaluate the apparent viscosity of shear-thinning bioinks have excessively relied on a simplified model, the Power Law model. The major drawback of this model is that the apparent viscosity unrealistically diverges to infinity at the low-shear-rate region [33,35,36]. To the authors' best knowledge, a more advanced and accurate model, such as the Bird-Carreau and Cross Power Law models, has not been explored for simulating polymer ink/bioink dynamics inside cylindrical printheads for extrusion-based 3D bioprinting. Machine learning approaches to predict cell viability also exist. A previous study utilised regression and classification neural networks to predict cell viability

based on parameters such as cell type, printing pressure, and crosslinker concentration, marking the cell type as the most influential permutation importance; however, the models were trained mainly based on limited datasets from other literature which affect model performance and precision [37]. Nevertheless, a generalised approach combining experiments, simulations, and machine learning models that can accurately predict cell viability based on the magnitude of shear stress and duration of such shear stress for diverse cell lines for rapid bioink formulation optimisation has not been reported before.

To address these gaps, this study aims to develop a novel, integrated framework that combines advanced rheological modelling, high-fidelity CFD simulations, and machine learning techniques to comprehensively evaluate and predict as-extruded cell viability. Specifically, this study utilises alginate-based bioink to evaluate shear stress effects on cell viability during the extrusion process as a generalisable model system for understanding and optimising cell survival in extrusion-based bioprinting. By characterising the relationship between shear stress, exposure time, and cell viability for different cell types, the framework enables rapid prediction and optimisation of cell viability for new bioink formulations, eliminating the need for extensive experimental testing of each new bioink composition.

To generalise the findings and ensure the broad applicability of the framework, four representative and diverse cell lines were selected in this study: immortalised human umbilical vein endothelial (HUEhT-1) cells, human cervical cancer (HeLa) cells, human bone marrow-derived mesenchymal stem (UE7T-13), and mouse embryonic fibroblast C3H/10T1/2-clone 8 (10T1/2) cells. The selections were motivated by their diverse origins – endothelial, cancerous, fibroblast, and stem cells, respectively. HUEhT-1 cells can help study endothelial cells' behaviour in vascular structures and cardiac tissue replacement [38]. HeLa cells are essential for researching tumour environments and the dynamics of cancer cells [39]. UE7T-13 cells are crucial for studying the differentiation and regenerative potential of mesenchymal stem cells (MSCs) in various tissue engineering applications [40]. 10T1/2 cells can model connective tissue and assist in understanding the integration and function of fibroblasts in tissue regeneration applications [41].

To accurately predict apparent viscosities for modelling shear stress, support vector regression (SVR) is employed to predict alginate inks' Cross Power Law model parameters. SVR is selected for its robustness in providing accurate predictions with small sample sizes and maximising predictive accuracy by computing confidence intervals of variable importance [42]. The predicted Cross Power Law parameters are then utilised in CFD simulations to evaluate the shear stress distribution inside the printhead. The simulation results and experimental cell viability data are used to train multilayer perceptron (MLP) regressors, a type of feedforward neural network, for predicting cell-type-dependent viability. MLP regressors are chosen for their ability to capture the intricate non-linear relationship among shear stress, exposure time to shear stress, and cell viability for different cell types, as they can learn complex patterns from cell-type-specific data and handle the interaction effects between multiple variables [43,44].

This study presents a quantitative framework for predicting and optimising as-extruded cell viability in extrusion-based 3D bioprinting. The framework incorporates high-accuracy predictive models for ink rheology and as-extruded cell viability across multiple cell types, enhancing the precision of apparent viscosity modelling for shear-thinning bioinks. Experimental validation also confirms the framework's effectiveness in optimising composite bioink formulations and extrusion parameters to achieve optimal cell viability. Consequently, this generalisable prototyping framework can enhance the precision of formulating bioink concentrations and tailor extrusion rates by examining the maximum allowable shear stress and the exposure time range at a desirable cell viability threshold. Such a framework can swiftly adapt to other bioink formulations, expediting the optimisation of printing parameters for diverse tissue engineering applications.

2. Materials and methods

2.1. Viscosity measurement

Sodium alginate (I-1G; mannuronic acid/guluronic acid ratio ≈ 0.7; molecular weight ≈ 70 kDa; Funakoshi Co., Ltd., Tokyo, Japan) was dissolved in phosphate-buffered saline (PBS (-); pH = 7.4) to form alginate (ALG) ink. A rheometer (HAAKE MARS III; Thermo Fisher Scientific Inc., Waltham, MA, USA) with a 40 mm parallel plate geometry was used for viscosity measurements. Viscosity measurements were conducted for ALG inks, ranging from 1.0 to 6.5% (w/v) at 4, 10, 20, 25, 30, 37, and 45 °C. Shear rates ranging from 0.01 to 1000 s^{-1} were applied for 360 s at a gap size of 0.5 mm.

2.2. Empirical viscosity model selection

Three generalised Newtonian fluid models, the Power Law model, the Bird-Carreau model, and the Cross Power Law model, were evaluated to identify the optimal empirical viscosity model for ALG inks.

The Power Law is defined as

$$\eta(\dot{\gamma}) = K\dot{\gamma}^{n_{PL}-1} \tag{1}$$

where $\dot{\gamma}$ is the shear rate, $\eta(\dot{\gamma})$ is the apparent viscosity as a function of the shear rate, K is the consistency index, and n_{PL} is the flow index [45].

The Bird-Carreau model is defined as

$$\eta(\dot{\gamma}) = \eta_\infty + (\eta_0 - \eta_\infty)(1 + (\lambda\dot{\gamma})^2)^{\frac{n_{BC}-1}{2}} \tag{2}$$

where η_∞ is the infinite-shear-rate viscosity, η_0 is the zero-shear-rate viscosity, λ is the characteristic time, and n_{BC} is the power index [46].

The Cross Power Law is defined as

$$\eta(\dot{\gamma}) = \eta_\infty + \frac{\eta_0 - \eta_\infty}{1 + (m\dot{\gamma})^n} \tag{3}$$

where m is the time constant, and n is the shear-thinning index [36,47,48]. Similar to the Bird-Carreau model, this model also assumes two Newtonian plateau regions at zero-shear-rate and infinite-shear-rate viscosities. For $n < 1$, the fluid exhibits shear-thinning behaviour; for $n = 1$, the fluid behaves Newtonian; for $n > 1$, the fluid displays shear-thickening behaviour [49]. The Cross Power fluid transitions from a zero-shear-rate region to an infinite-shear-rate region through two transition regions separated by the power law region with the slope of $-n$. The transitional shear rate in transition region one is denoted by $\dot{\gamma} = 1/m$. The typical apparent viscosity profile for a Cross Power Law shear-thinning fluid is illustrated in Figure 1.

Curve fittings of each experimental apparent viscosity profile were acquired through non-linear least squares regression with Python (version 3.12.3) scripts that employ SciPy (version 1.13.1). Root mean square error (RMSE) was used for error evaluation and model selection. RMSE is defined as

$$\text{RMSE} = \sqrt{\frac{1}{n}\sum_{i=1}^{n}(y_i - \hat{y}_i)^2} \tag{4}$$

where y_i are the observed values, $\hat{y}_i$ are the predicted values, and n is the number of observations. The Cross Power Law was selected as the optimal empirical model, which will be discussed in Section 3.1.

2.3. Viscosity predictive modelling via support vector regression (SVR)

To accurately model the rheological parameters of ALG inks under varying concentrations and temperatures, SVR, developed using Scikit-learn (version 1.5.0), was used for predicting the Cross Power Law parameters for any given concentration and temperature within the experimental range. It was concluded from the fitting process that as long as η_∞ is small and less than 10^{-3} Pa·s, the changes in other Cross Power Law parameters (η_0, m, and n) are negligible. To simplify the problem and improve numerical stability in CFD simulations, η_∞ was assumed to be a minimal and constant number at 10^{-3} Pa·s for all concentrations and temperatures.

Each fitted Cross Power Law parameter contained 76 data points. Data of fitted parameters were first scaled to have zero mean and unit variance. Logarithmic transformations were then applied to the scaled data to account for the wide range of fitted parameter values. The radial basis function (RBF) kernel was used to capture the non-linear relationships between the input and output features by mapping the data to an infinite-dimensional space [50]. The best model was selected based on a grid search for hyperparameter tuning. The selection criterion of the hyperparameters was based on the lowest 20-fold cross-validated mean

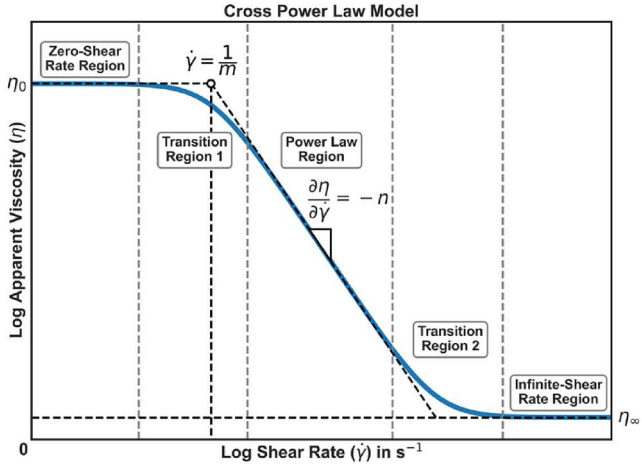

Figure 1. Apparent viscosity as a function of shear rate for a hypothetical shear-thinning fluid exhibiting Cross Power Law behaviour.

squared error (MSE) for each output feature. The choice of 20 folds was based on the small dataset size to provide a more reliable and less biased estimate of the model's performance. MSE is defined as

$$\mathrm{MSE} = \frac{1}{n}\sum_{i=1}^{n}(y_i - \hat{y}_i)^2 \tag{5}$$

The grid search explored a range of hyperparameters, the regularisation parameter (C), kernel coefficient (γ), and epsilon-tube width (ϵ) to find the optimal combination that minimised the MSE. To further understand the performance of the best model, the 20-fold cross-validated coefficient of determination (R^2) and mean absolute error (MAE) were calculated. The coefficient of determination is defined as

$$R^2 = 1 - \frac{\sum_{i=1}^{n}(y_i - \hat{y}_i)^2}{\sum_{i=1}^{n}(y_i - \bar{y})^2} \tag{6}$$

where $\bar{y}$ is the mean of the observed data. The mean absolute error is defined as

$$\mathrm{MAE} = \frac{1}{n}\sum_{i=1}^{n}|y_i - \hat{y}_i| \tag{7}$$

2.4. Ink rheological stability measurement

To evaluate the rheological stability of the ALG inks with concentrations ranging from 2.0 to 6.5% (w/v) at room temperature (22.5 °C), a contact angle metre (LSE ME3; NiCK Corporation, Saitama, Japan) was used to measure contact angles with a time elapsing range from 0 to 45 s. A suspending ink droplet of 1.0 µL was extruded from a 27-gauge cylindrical needle printhead (PN-27G-B; Musashi Engineering, Inc., Tokyo, Japan), and a polystyrene substrate was lifted to collect the droplet. The contact angle measurement started when the droplet completely separated from the needle tip.

2.5. Cell culture

HUEhT-1, HeLa, UE7T-13, and 10T1/2 cell lines were sourced from Riken Cell Bank (Riken BioResource Research Center, Ibaraki, Japan). For the HUEhT-1 cell line, MCDB107 medium (Research Institute for the Functional Peptides Co., Ltd, Osaka, Japan) with 10% (v/v) fetal bovine serum (FBS), 10 ng/mL endothelial growth factor, and 10 ng/mL basic fibroblast growth factor (both from Sigma-Aldrich, St. Louis, MO, USA) was used for cell culturing. For HeLa, UE7T-13, and 10T1/2 cell lines, low glucose Dulbecco's modified Eagle medium (DMEM) (Shimadzu Diagnostics Corporation, Tokyo, Japan) with 10% (v/v) FBS was used instead. Cells were cultured in a humidified incubator at 37 °C supplied with 5% carbon dioxide (CO_2).

2.6. As-extruded cell viability evaluation

Cells were harvested from cell culture dishes through trypsinization and suspended in 4.0 to 6.5% (w/v) ALG ink at 1.0×10^6 cells/mL. The bioinks were filled in 2.0 mL plastic syringes and extruded from 27-gauge cylindrical needle printheads by a syringe pump (PHD 2000; Harvard Apparatus, Holliston, MA, USA) with extrusion rates of 1.0, 1.5, 2.0, and 3.0 µL/s at 22.5 °C. The cylindrical needle has an inner diameter of 0.2 mm and a length of 20 mm. The cells inside the extruded inks were stained with calcein-acetoxymethyl (calcein-AM) (Nacalai Tesque, Inc., Kyoto, Japan) and propidium iodide (PI) (Dojindo Laboratories Co., Ltd, Kumamoto, Japan) both at 3.33 µg/mL in PBS (-); fluorescence images of each sample were taken by a fluorescence microscope (APX100; Olympus Corporation, Tokyo, Japan). Python scripts that employed OpenCV (version 4.9.0) were used to analyze each image and determine corresponding as-extruded cell viability (also referred to as cell viability in this study).

2.7. Numerical simulation

CFD simulations were implemented for ALG inks with concentrations ranging from 2.0 to 6.5% (w/v) at 4 to 45 °C inside the 27-gauge cylindrical needle printhead. The density of the ink was approximated as 1.0×10^3 kg/m^3. The inlet flow rates ranged from 0.5 to 3.5 µL/s. The numerical model incorporated the following assumptions:

(I) Inks are isothermal and incompressible, exhibiting non-Newtonian behaviour modelled by the Cross Power Law.
(II) The flow is axisymmetric, steady-state, and fully developed. Due to the needle printhead's micro-scale and low Reynolds number, the flow is laminar with a negligible entrance length.
(III) Gravitational effects are negligible compared to viscous forces.

Fidelity Pointwise (version 18.6 R6; Cadence Design Systems, Inc., San Jose, CA, USA) was employed for mesh generation. The dimension of the simulation domain is based on the polymer ink region in the computer-aided design (CAD) model and engineering drawing shown in Figure 2(a,b). A constant flow rate Q was applied to the inlet, and a no-slip wall boundary condition ($\boldsymbol{U}_{\mathrm{wall}} = 0$) was applied to the wall. At the outlet, the pressure was set to a reference value $P_{\mathrm{out}} = 0$. Wedge boundary conditions were applied to the sides of the structured mesh with a rotation angle of 5 degrees, as

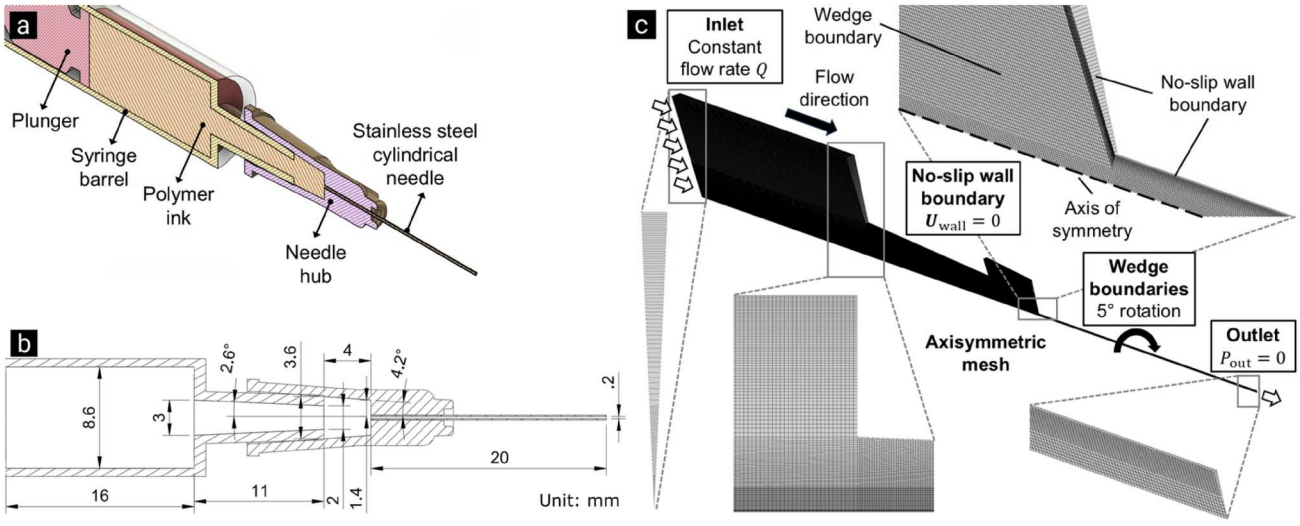

Figure 2. (a) Cross-sectional view of the 27-gauge cylindrical needle printhead attached to the syringe. (b) Engineering drawing of the syringe and cylindrical needle printhead. (c) Schematic diagram of the simulation mesh and boundary conditions.

illustrated in Figure 2(c). The wedge boundary conditions were used to reduce computational costs by limiting the simulation domain to two-dimensional space in the axial and radial directions [51].

Mesh dependency tests were conducted by evaluating wall shear stress and average velocity at the needle outlet. The two parameters at the needle outlet achieved stable convergence after the number of elements in the mesh reached 3.0×10^4, as shown in the Appendix (Figure A1). The number of elements was selected at around 4.0×10^4 to balance simulation accuracy and computational time. The Cross Power Law was used as the rheology model in the simulations, and the parameters for the simulations were predicted via the SVR models. The simulations utilised the finite volume method via OpenFOAM (version 11; The OpenFOAM Foundation, London, UK), an open-source computational fluid dynamics software [52]. The semi-implicit method for pressure linked equations-consistent (SIMPLEC) algorithm was used to solve the governing equations iteratively. Simulation convergence was achieved when the relative residuals of the velocity vectors and pressure field dropped below 10^{-5}. The governing equations of the simulations are listed as follows:

Incompressible continuity equation:

$$\nabla \cdot \boldsymbol{U} = 0 \tag{8}$$

where $\boldsymbol{U}$ is the velocity vector.

Steady-state Navier–Stokes equations:

$$\boldsymbol{U} \cdot \nabla \boldsymbol{U} - \nabla \cdot (\nu \nabla \boldsymbol{U}) = -\nabla p \tag{9}$$

where ν is the kinematic viscosity and p is the kinematic pressure.

The shear rate is defined as

$$\dot{\gamma} = \sqrt{\frac{1}{2} \nabla \boldsymbol{U} : \nabla \boldsymbol{U}} \tag{10}$$

The cell residence time, or exposure time, inside the cylindrical needle was considered to evaluate the influence of shear stress duration on cell viability. The exposure time is defined as

$$t_{\text{exposure}} = \frac{L_{\text{needle}}}{\bar{U}_{\text{needle}}} \tag{11}$$

where t_{exposure} is the exposure time, L_{needle} is the needle length, and $\bar{U}_{\text{needle}}$ is the average flow velocity inside the needle.

To validate the simulation results, an analytical approach was used to solve the Cross Power Law inside the cylindrical needle iteratively. For a pressure-driven, axisymmetric, laminar pipe flow, the radial momentum balance equation, which defines the pressure gradient, is given by:

$$\frac{dp}{dz} = \frac{1}{r} \frac{d}{dr} \left(r \eta(\dot{\gamma}) \frac{du_r}{dr} \right) \tag{12}$$

where r is the radial position, and u_r is the radial velocity. The pressure gradient inside the cylindrical needle was obtained from the simulation result. For each radial position r, the velocity gradient was computed from the previously known velocity.

The shear stress (τ) as a function of the radial position was calculated based on

$$\tau(r) = \eta(r) \dot{\gamma}(r) \tag{13}$$

2.8. Cell viability predictive modelling via multi-layer perceptron (MLP) regressors

Wall shear stress, defined as the shear stress magnitude at the wall, was considered because it serves as a fixed parameter, providing a consistent measure for modelling purposes. MLP regressors were utilised to model cell viability based on wall shear stress ranging from 1.0 kPa to 5.0 kPa and exposure time ranging from 100 ms to 700 ms for each cell type. These ranges closely resembled the experimental and simulation data and avoided extrapolating to regions far from the collected data, ensuring the model's reliability and applicability [53]. MLP regression models were developed via Scikit-learn. The neural network was trained using datasets containing wall shear stress, exposure time, and corresponding cell viability values obtained from both simulations and experiments. Before training, data were scaled to have zero mean and unit variance. To identify the optimal MLP architecture, a grid search was employed for hyperparameter tuning. The hyperparameters include the number of hidden layers, the number of neurons in each hidden layer, and the ridge regularisation coefficient (α). The activation function used in the hidden layers was the rectified linear unit (ReLU). 'Adam,' an algorithm for first-order gradient-based optimisation of stochastic objective functions, was used as the weight and bias optimisation solver [54]. The learning rate was set to be constant at 0.001. The explored hidden layer architectures varied from single-layer networks (16–256 neurons) to two-layer networks ((16, 16) to (128, 128) neurons) to find the optimal balance between model capacity and generalisation performance. The model's performance was evaluated based on the lowest 20-fold cross-validated MSE. To validate the optimal model, 20-fold cross-validated R^2, MAE, and RMSE were calculated. The trained MLP regressors model can predict cell viability for a given combination of cell type, wall shear stress, and exposure time within the specified ranges.

2.9. Cell viability predictive model validation

To validate the MLP regression models and confirm their applicability, sodium alginate was mixed with sodium hyaluronate (HA-LQ; molecular weight $\approx$ 85-100 kDa; Kewpie Corporation, Tokyo, Japan) in PBS(-) to form ALG and hyaluronic acid (HA) composite inks. Three formulations were tested: ALG4-HA1, ALG4-HA1.5, and ALG4-HA2, where the numbers indicate the concentration (w/v%) of each component. Viscosity measurements for each composite ink were conducted at 22.5 °C as described in Section 2.1. Due to the limited number of samples, SVR models were not developed for these composite inks; instead, the Cross Power Law fitted experimental viscosity data at 22.5 °C were explicitly used for numerical simulations to evaluate shear stress and exposure time. As-extruded cell viability evaluation experiments were conducted as described in Section 2.6.

3. Results

3.1. Comparison and selection of rheological models

Representative comparisons of fitted viscosity and shear stress profiles for 4.0% (w/v) ALG using the Power Law, Bird-Carreau, and Cross Power Law models are shown in Figure 3. The Power Law model diverged rapidly at a shear rate of around 10 s^{-1} and lower, indicating a significant deviation from experimental data in the low-shear-rate region. Conversely, the Bird-Carreau model underestimated the zero-shear-rate viscosity, leading to inaccuracies in predicting the material's behaviour under low-shear conditions. The Cross Power Law model provides the lowest RMSE and a smooth viscosity and shear stress transition across the entire experimental shear rate spectrum.

3.2. Trained SVR models for viscosity prediction

The trained SVR model predicts the Cross Power Law parameters based on ALG inks' concentrations and temperatures. The optimal SVR hyperparameters for each Cross Power Law parameter are listed in Table 1.

The prediction surfaces for zero-shear rate viscosity (η_0), time constant (m), and shear-thinning index (n) are illustrated in Figure 4(a–c). η_0 and m increased exponentially as the concentration of the ink increased, leading to an overall increase in apparent viscosity and a decrease in the transitional shear rate ($1/m$). n increased rapidly at a concentration below 3.0% (w/v); however, the rate of increase decayed after 3.5% (w/v). All three parameters increased when the ink temperature decreased. The optimal model's 20-fold cross-validated R^2 for η_0, m, and n are 0.985, 0.949, and 0.952, respectively, as shown in Figure 4(d–f). The cross-validated results indicate that the trained models achieve generalisation and high prediction accuracy. Comparisons between ALG inks' experimental data and SVR prediction curves to confirm the model's performance in action are shown in Figure 4(g–h). A close alignment was observed between experimental data and SVR-predicted viscosity curves.

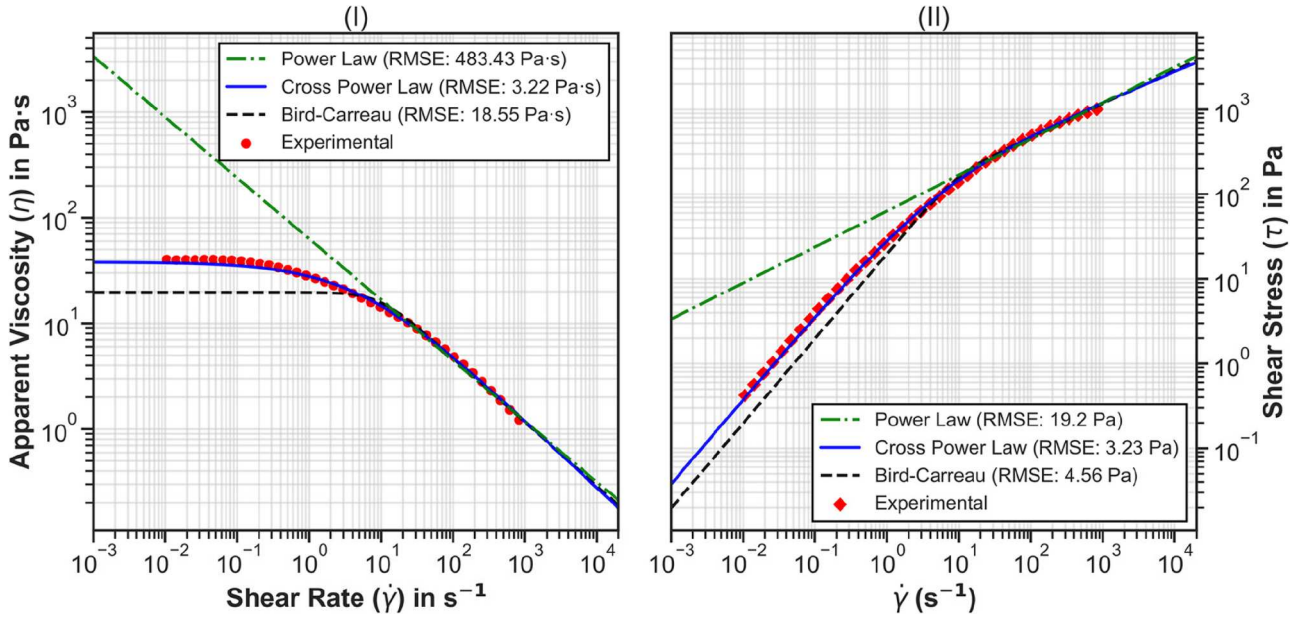

Figure 3. Non-linear regression fittings using the Power Law, Cross Power Law, and Bird-Carreau models for 4.0% (w/v) ALG at 25 °C. (I) Apparent viscosity; (II) Shear stress. RMSE: root mean squared error.

3.3. Ink rheological stability characterisation

Time-elapsing images from 0 to 45 s of the contact angles for ALG inks ranging from 2.0 to 6.5% (w/v) are shown in Figure 5(a), indicating that the ink rheological stability increases with the ink concentrations. Inks at all concentrations experienced a rapid decrease in contact angle within the first 5 s measurement interval and converged to distinct contact angles after 15–45 s, with higher-concentration inks exhibiting higher and more stable contact angles, as depicted in Figure 5(b).

3.4. Ink flow and shear stress characterisation

The representative comparisons between analytical and simulation results are shown in the Appendix (Figure A2). The close agreement between the analytical and simulation results suggests the accuracy and reliability of the CFD simulations. Representative contour plots of static pressure, velocity field, apparent viscosity, shear rate, and shear stress inside the needle printhead are shown in Figure 6(a–e). The pressure drop, flow velocity, shear rate, and shear stress inside the syringe barrel and needle hub were negligible compared to the region around the cylindrical needle. The pressure inside the syringe began to drop only upon entering the cylindrical needle, as illustrated in Figure 6(a). The region where the velocity magnitude was significant was within the cylindrical needle, as shown in Figure 6(b). The apparent viscosity decreased rapidly as the fluid entered the cylindrical needle, confirming the shear-thinning property of the ink when applying high shear rates, as shown in Figure 6(c). In addition, the applied shear rate inside the printhead could be as low as in the 10^{-6} s^{-1} magnitude, as shown in Figure 6(d). Furthermore, the extensional stress had a similar magnitude compared to wall shear stress, although the affecting length (0.2 mm) was much shorter than wall shear stress (20 mm), as shown in Figure 6(e). In addition to cylindrical needles, simulations were also conducted for a tapered nozzle. The shear stress distribution for a tapered 27-gauge nozzle with 5.0% (w/v) ALG ink at 22.5 °C and an extrusion rate of 1.5 µL/s is shown in the Appendix (Figure A3). The simulation revealed higher shear stress distribution near the nozzle exit than the wall shear stress inside the cylindrical needle; however, the exposure time and distance to such shear stress are much shorter than the cylindrical needle.

The magnitude of wall shear stress at varying ink concentrations and extrusion rates at 22.5 °C is shown in Figure 7(a). Rising extrusion increased wall shear stress, which became more pronounced as the concentration increased. The effect of changing temperature and

Table 1. 20-fold validated optimal SVR hyperparameters for each Cross Power Law parameter.

Cross Power Law parameter	Regularisation parameter (C)	Kernel coefficient (γ)	Epsilon-tube width (ε)
Zero-shear-rate viscosity (η_0)	780	0.0750	0.04250
Time constant (m)	560	0.0750	0.05875
Shear-thinning index (n)	120	0.0425	0.04250

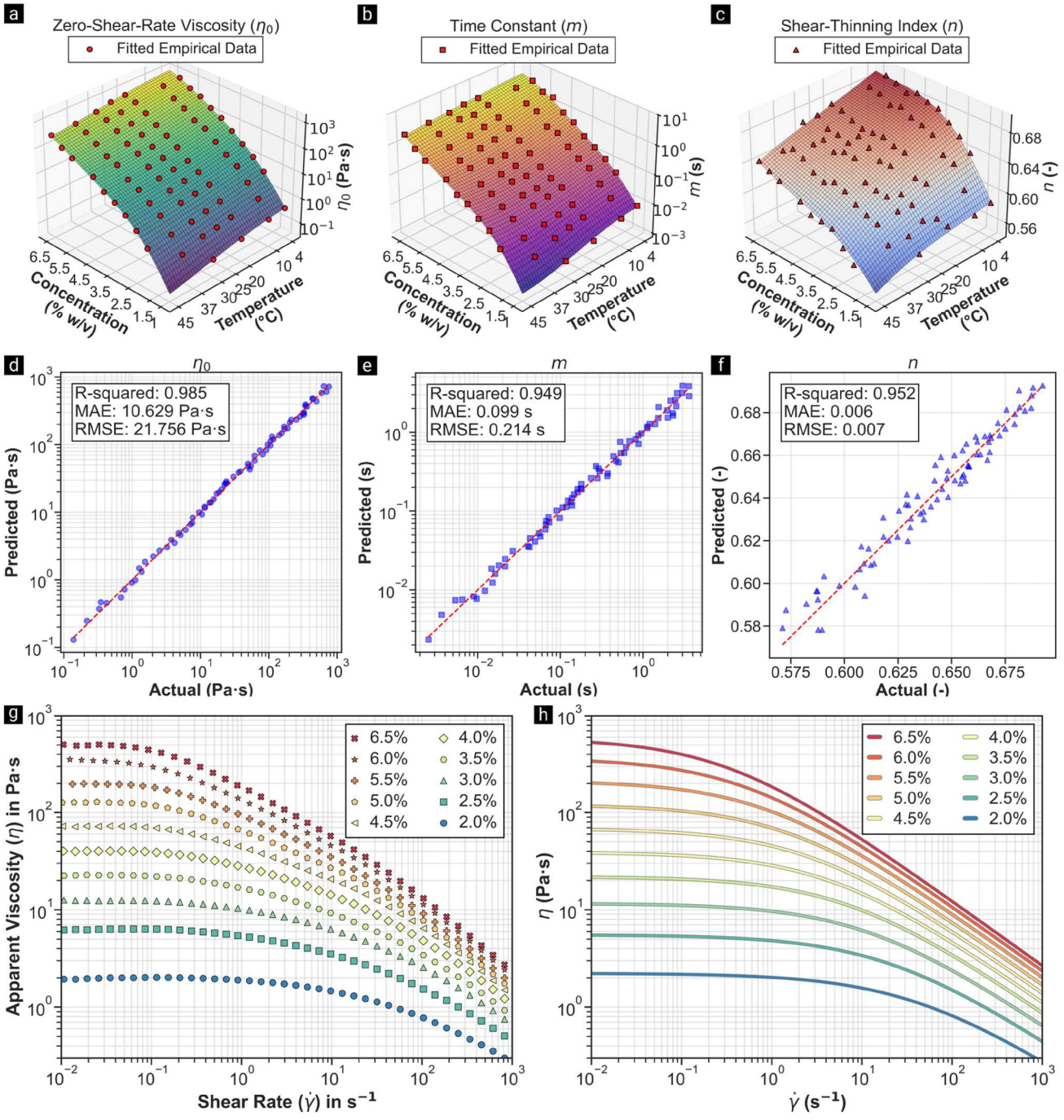

Figure 4. Prediction surfaces and fitted empirical data points for Cross Power Law parameters (a) η_0, (b) m, and (c) n. 20-fold cross-validation results for (d) η_0, (e) m, and (f) n. R-squared: coefficient of determination. MAE: mean absolute error. Apparent viscosity vs. shear rate profiles for ALG inks ranging from 2.0 to 6.5% (w/v) at 25 °C: (g) experimental data and (h) SVR-predicted Cross Power Law viscosity curves.

extrusion rate on wall shear stress is depicted in the Appendix (Figure A4a–c). Increasing the temperature from 4 °C to 22.5 °C had little impact on wall shear stress across all concentrations. However, a significant reduction in wall shear stress was observed when the temperature was increased to 37 °C from 22.5 °C, particularly for higher-concentration inks. The correlation matrix for ink concentration, temperature, η_0, m, n, wall shear stress (τ_{wall}), pressure drop (ΔP), and average flow velocity inside the needle ($\bar{U}_{needle}$) is shown in Figure 7(b). η_0, m, and n all exhibited strong dependences on ink concentration and temperature, although n was more sensitive to temperature change than η_0, m. The magnitude of wall shear stress and pressure drop strongly correlated with the ink concentration; they were directly proportional to each other, indicating an identical trend in response to varying flow conditions.

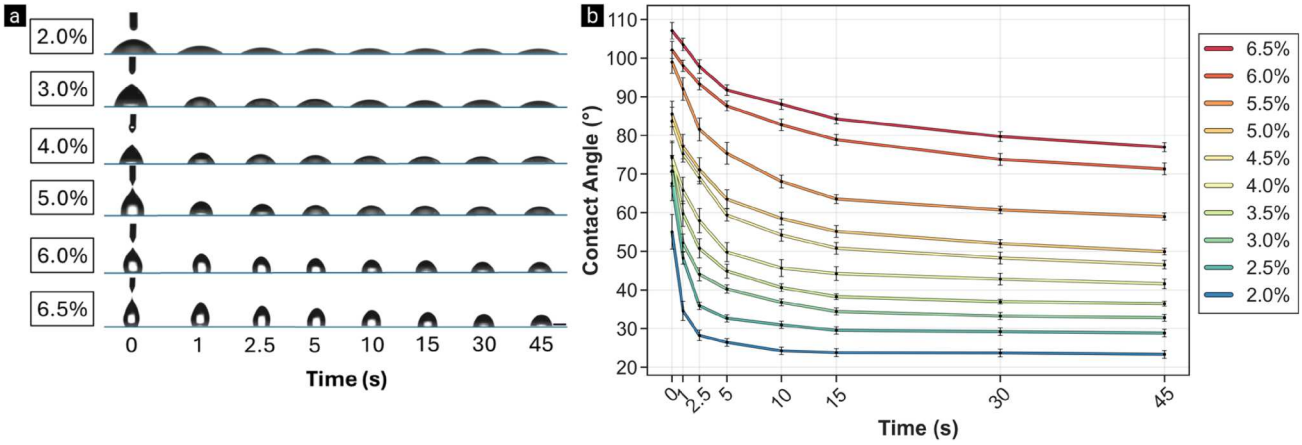

Figure 5. (a) Contact angle time elapsing images and (b) line plot for 2.0–6.5% (w/v) ALG inks from 0 to 45 s at 22.5 °C. The scale bar indicates 1 mm. Data are mean ± standard deviation (S.D.), $n = 3$ for each data point.

3.5. Cell viability, wall shear stress, and exposure time characterisation

In preliminary experiments, no apparent decrease in cell viability (> 99%) was observed for each cell line when the ALG concentration in the bioink was at or below 3.5% (w/v) (data not shown). Thus, cell viability was investigated using inks with ALG concentrations ranging from 4.0% to 6.5% (w/v). The cell viability was investigated based on the fluorescence microscopy of the cells stained with Calcein-AM (green) and PI (red) (Figure 8(a)), which stained the live and dead cells, respectively.

Cell viability line plots at ink concentrations ranging from 4.0 to 6.5% with extrusion rates ranging from 1.0 to 3.0 µL/s for 10T1/2, UE7T-13, HeLa, and HUEhT-1 cells are shown in the Appendix (Figure A5). With an extrusion rate of 1.5 µL/s, the viability of HUEhT-1 cells remained above 90.2 ± 2.9% at 4.0% (w/v) but decreased extensively as ink concentration increased; the viability of HeLa cells remained robust (> 94.7 ± 1.5%) at and below 5.0% (w/v), and UE7T-13 cells maintained high cell viability (> 95.2 ± 2.6%) at and below 4.5% (w/v). In contrast, the viability of 10T1/2 cells (> 93.2 ± 2.6%) remained at and below 6.0% (w/v). Increasing the extrusion rate did not apparently affect cell viability; in some cases, decreasing extrusion could result in lower cell viability.

To further generalise and understand the findings, wall shear stress and exposure time data obtained from simulations were combined with the experimental cell viability data at varying concentrations and extrusion rates. 3D cell viability line plots were generated for each cell line, as shown in Figure 8(b–e). The plots revealed that cell viability decreased by increasing wall shear stress and exposure time. Cell viability decreased as the exposure time increased for a similar wall shear stress magnitude. The degree of reduction in cell viability varied substantially among the four cell lines, with HUEhT-1 cells being the most sensitive to shear stress and exposure time, followed by UE7T-13, HeLa, and 10T1/2 cells.

3.6. Trained MPL regression models for cell viability prediction

MLP regressors were trained on the results obtained from experiments and simulations. The optimal MLP regressor hyperparameters for each cell type are listed in Table 2.

The cell viability surface plots for each cell line are depicted in Figure 9(a–d). Cell viability decreased much more rapidly in the higher-stress region than in the lower-stress region. Higher exposure time resulted in lower cell viability. 20-fold cross-validated R^2 of optimal models for 10T1/2, UE7T-13, HeLa, and HUEhT-1 cell lines are 0.866, 0.964, 0.916, and 0.956, respectively, as shown in Figure 9(e–h). The cross-validated results suggest that the trained models achieve high prediction accuracy and generalisation. To further understand and visualise the influence of constant wall shear stress on cell viability, exposure time vs. cell viability plots under constant wall shear stress ranging from 1.0 to 5.0 kPa were established for each cell line, as shown in Figure 9(i–l). As exposure time increased, cell viability decreased noticeably, particularly with higher wall shear stress magnitudes.

3.7. Cell viability predictive model validation

Composite bioinks consisting of ALG and HA were used to evaluate the model's capability on different bioink formulations. The MLP regression models demonstrated excellent performance in predicting cell viability when

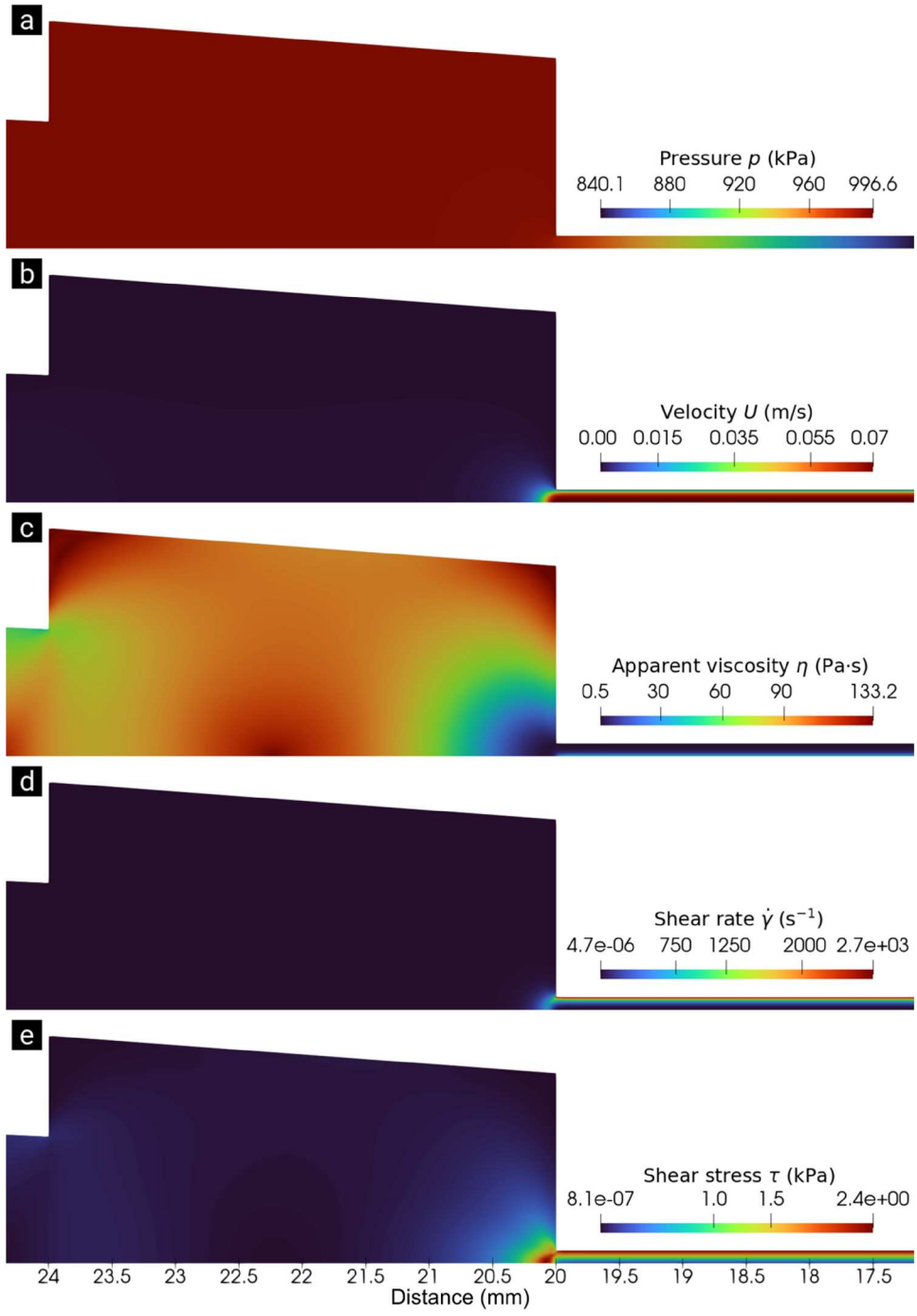

Figure 6. CFD characterisations of 5.0% (w/v) ALG ink at 22.5 °C with an extrusion rate of 1.5 µL/s inside the cylindrical 27-gauge needle printhead. (a) static pressure, (b) velocity field, (c) apparent viscosity, (d) shear rate, and (e) shear stress.

applied to the composite ALG-HA bioinks. The viscosity data of composite ALG-HA polymer inks are shown in the Appendix (Figure A6). The fluorescence microscopy of the cells stained with Calcein-AM and PI is shown in Figure 10(a). The comparison between experimental results and model predictions for the ALG-HA formulations at different extrusion rates is shown in Figure 10(b). The comparison between observed and predicted cell viability is presented in Table 3. The mean absolute error (MAE) ranged from 0.96% to 8.13%, with larger discrepancies occurring at 1.0 µL/s extrusion rates.

3.8. Cell viability optimisation

The overlaid surface plot that compares the cell viability for each cell line under the influence of wall shear stress and exposure time is depicted in Figure 11(a). Apparent deviations in cell viability are observed across 10T1/2,

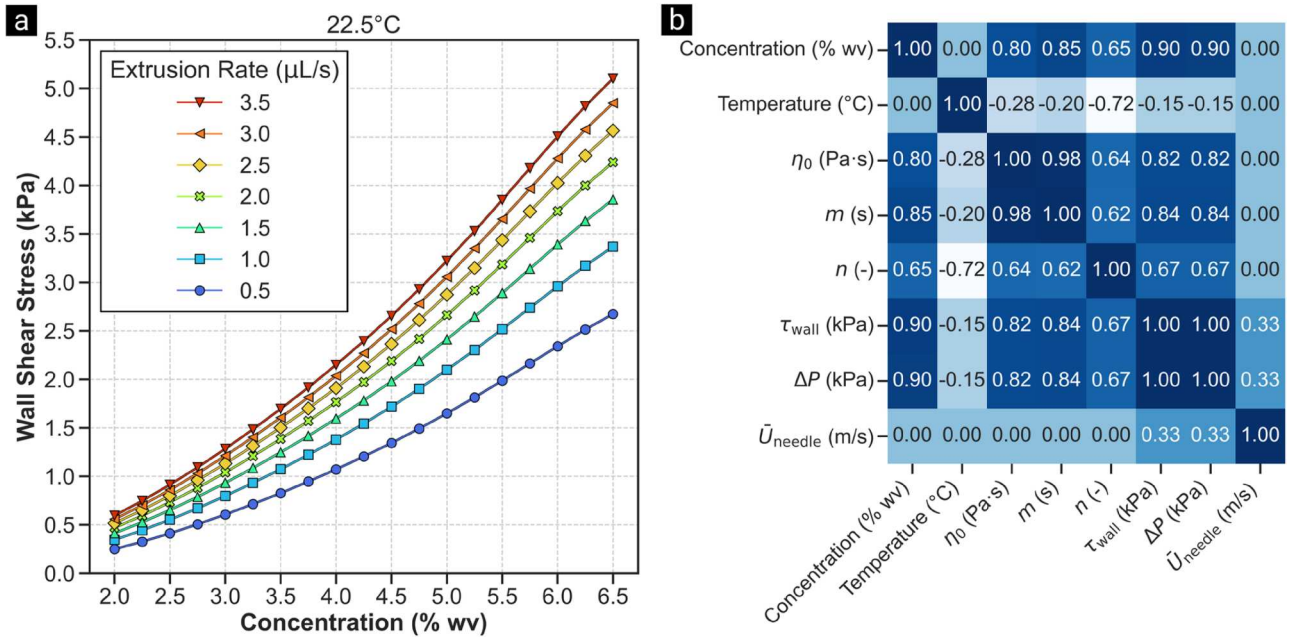

Figure 7. (a) ALG ink concentration vs. wall shear stress with extrusion rates range from 0.5 to 3.5 μL/s at 22.5 °C. (b) Correlation matrix of the simulation parameters and results. Correlation values range from −1 to 1, where 1 indicates a perfect positive correlation, −1 indicates a perfect negative correlation, and 0 indicates no correlation.

UE7T-13, HeLa, and HUEhT-1 cell lines, indicating that cell viability is highly cell-type dependent. To characterise the effect of wall shear stress and exposure time on cell viability after extrusion, a contour plot with 90% to 50% cell viability threshold lines is shown in Figure 11 (b–e). When considering the full range of exposure times from 100 to 700 ms, the maximum acceptable wall shear stress to maintain 80% viability varied among cell types. For HUEhT-1 cells, the maximum acceptable wall shear stress was 1.57 kPa, while for HeLa, UE7T-13, and 10T1/2 cells, it was 1.99 kPa, 2.33 kPa and 3.14 kPa, respectively. Noticeably, 10T1/2 cells exhibited a distinct turning point at around 3.90 kPa, where the exposure time must be reduced to below 300 ms to maintain above 80% cell viability. Taking 400 ms exposure time as a representative example, the viability of HUEhT-1 cells dropped to 80% at a wall shear stress of 2.05 kPa. In contrast, UE7T-13, HeLa, and 10T1/2 cells showed similar decreases in viability at higher wall shear stress values of 2.65, 2.85, and 3.72 kPa, respectively, for the same exposure time.

4. Discussion

This study aims to develop a generalisable framework for predicting and optimising as-extruded cell viability in extrusion-based 3D bioprinting by integrating experimental data, CFD simulations, and machine learning models. A 27-gauge cylindrical needle was chosen due to its ability to achieve high printing resolution. Similar needle sizes are commonly used in extrusion-based bioprinting applications [17,21,55], allowing for meaningful comparisons with existing literature. While the experiments and simulations focused on this specific needle size for maintaining consistency, the framework is designed to be adaptable to various needle diameters. This adaptability can be achieved by modifying the simulation mesh geometry in the CFD simulations.

To accurately model the rheological properties of polymer inks for CFD simulations, the Power Law, the Bird-Carreau, and the Cross Power Law were compared. The Cross Power Law was selected as the optimal model due to the higher accuracy and lower RMSE in describing the rheological properties of ALG inks than the Power Law and Bird-Carreau models in both low and high shear rate regions (Figure 3). The CFD simulation results also showed that the shear rate inside the printhead could be as low as in the 10^{-6} s^{-1} magnitude (Figure 6(d)), which the Power Law model failed to capture accurately due to its divergence in the low-shear-rate region. In addition, the zero-shear-rate viscosity, time constant, and shear-thinning index provided by the Cross Power Law model offer a comprehensive understanding of bioink behaviour under different shear rates. In particular, the zero-shear-rate viscosity provides an intuitive way to understand ink viscosity at a low-shear-rate region; the time constant can be used to evaluate the transitional shear rate between the zero-shear-rate region and Power Law region; the

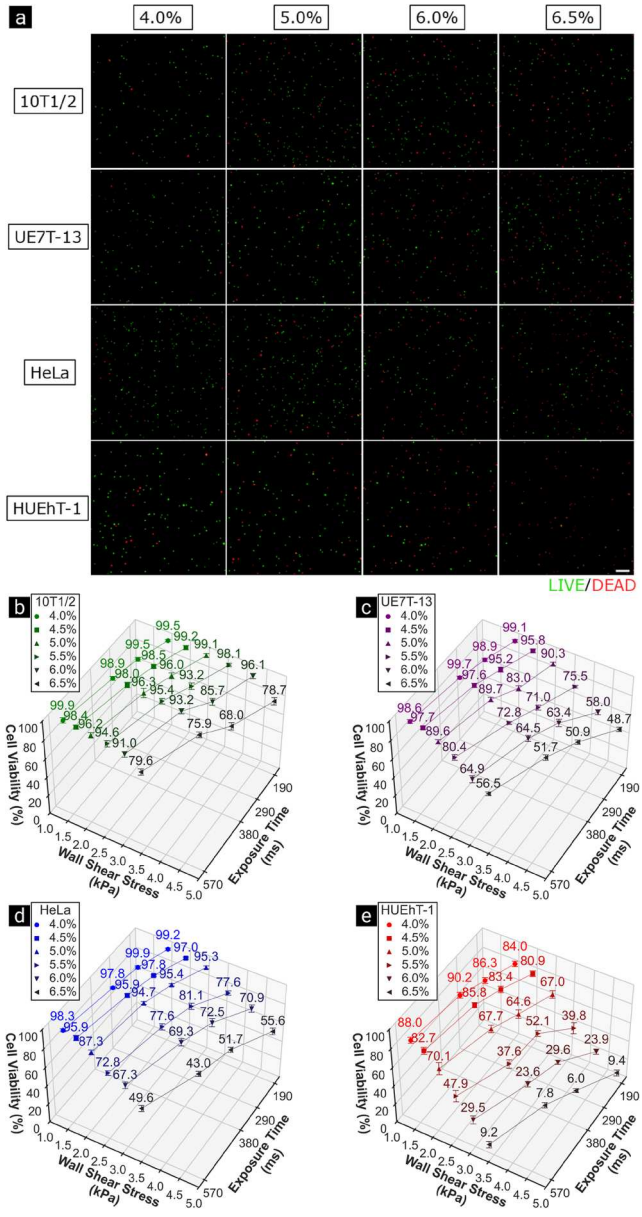

Figure 8. (a) Fluorescence images of LIVE/DEAD stained 10T1/2, UE7T-13, HeLa, and HUEhT-1 cells inside various ALG ink concentrations after extrusion at 1.5 µL/s. Green indicates live cells; red indicates dead cells. The scale bar indicates 200 µm. (b–d) Wall shear stress vs. exposure time vs. cell viability plots for (b) 10T1/2, (c) UE7T-13, (d) HeLa, and (e) HUEhT-1 cell lines. Data are mean ± S.D., $n \geq 8$ for each data point.

shear-thinning index can be directly used for quantifying the degree of shear-thinning behaviour. Furthermore, SVR models in this study provide a powerful way to generalise the viscosity profiles of inks at varying concentrations and temperatures (Figure 4(a,b)). While this study only considered inks at 22.5 °C, the SVR models can be applied in a wide range of temperatures from 4 to 45 °C. Such models have the potential to be extended to other inks, offering a versatile tool for predicting and controlling the rheological properties of diverse bioink formulations. Other inks, such as polyvinyl alcohol (PVA), HA, and ALG/gelatin composite inks, can also be described accurately by the Cross Power Law [56,57], as shown in the Appendix (Figure A7). Although the rheological data only considered polymer inks without cells, several studies have demonstrated that

Table 2. 20-fold validated optimal MLP regressor hyperparameters for each cell type.

Cell type	Number of data point	Architecture of the hidden layer	Ridge regularisation coefficient (α)
10T1/2	233	(64, 64)	0.150
UE7T-13	295	(128, 128)	0.329
HeLa	283	(128, 128)	1.286
HUEhT-1	239	(80, 80)	0.633

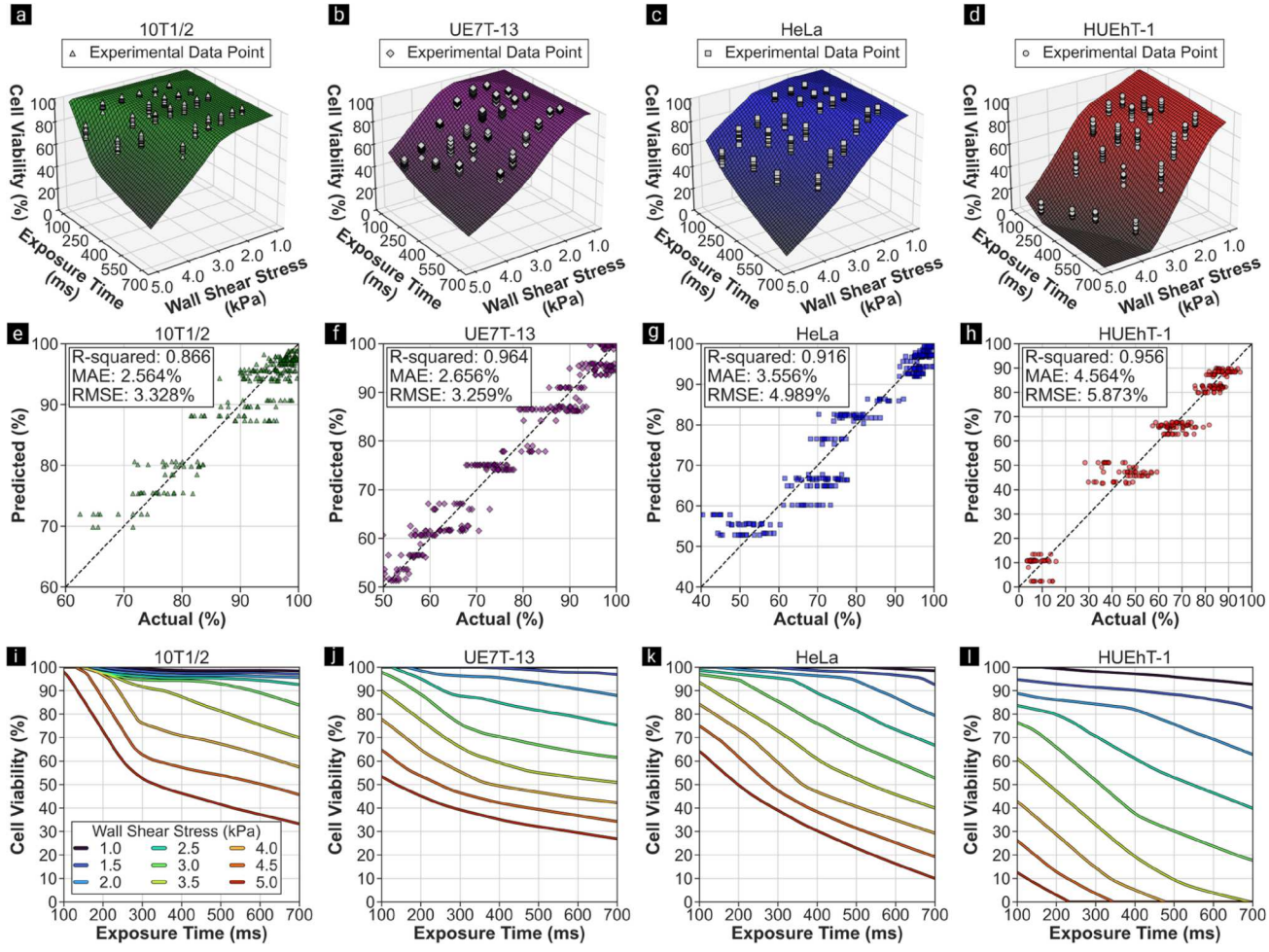

Figure 9. Surface prediction of cell viability plots for (a) 10T1/2, (b) UE7T-13, (c) HeLa, and (d) HUEhT-1 cells. (e–h) 20-fold cross-validation results for each cell line. (i–l) The predicted cell viability curve for each cell line with constant wall shear stress ranged from 1.0 to 5.0 kPa at exposure time ranging from 100 to 700 ms.

no significant differences were observed between the apparent viscosities of polymer ink and bioink, even with a high cell density at 19.5×10^6 cells/g [17,22,32].

Building upon the viscosity modelling results, ink rheological stability testing suggests that ink concentrations significantly affect the as-extruded stability of the extruded inks (Figure 5(a)). As the zero-shear-rate viscosity is highly correlated with the ink concentration, inks with higher zero-shear-rate viscosity are preferred to maximise ink stability. The rate of decrease in contact angle slowed as ink concentration increased (Figure 5(b)), indicating that higher-concentration inks exhibit more resistance to spreading. When printing layer-by-layer constructs, insufficient rheological stability can cause the ink to spread out, negatively affecting overall shape fidelity or even causing the construct to collapse [30]. Therefore, a large and slowly decreasing contact angle is desirable for maintaining the rheological stability of the printed construct. Nevertheless, for successful extrusion-based 3D bioprinting, ink rheological stability and cell viability should be considered simultaneously.

Subsequently, combining the results from CFD simulations and experimental cell viability data, the role of wall shear stress on the viability of fibroblast (10T1/2), mesenchymal stem (UE7T-13), cervical cancer (HeLa), and endothelial (HUEhT-1) cell lines was examined. Increasing the extrusion rate directly increased the magnitude of wall shear stress (Figure 7(a)). At first glance, the extrusion rate has little or no significant influence on cell viability; however, a clear trend can be observed once wall shear stress and exposure time are considered: increased exposure time decreases cell viability under a similar magnitude of wall shear stress (Figure 8(b–e)). The MLP regression models also confirmed this observation and further generalised the finding, predicting that higher exposure times at constant wall shear stress lead to lower cell viability for all four cell types (Figure 9(a–d, i–l)). This study confirms that exposure time is a critical factor affecting cell viability under

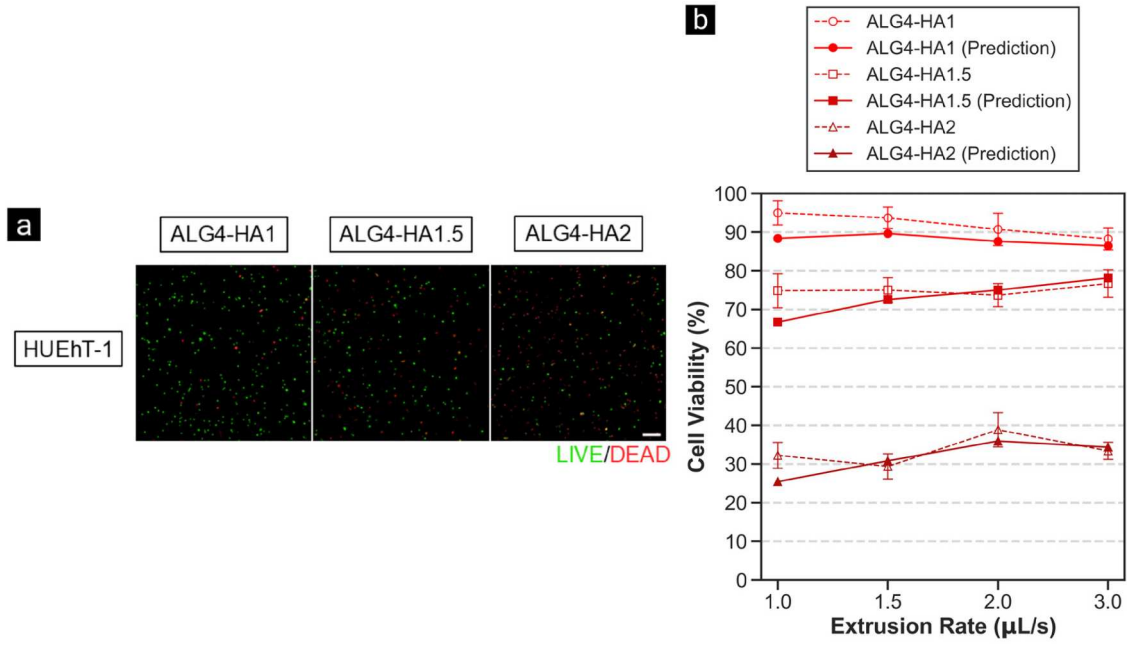

Figure 10. (a) Fluorescence images of LIVE/DEAD stained HUEhT-1 cells inside ALG-HA composite inks containing 4.0% (w/v) ALG and 1.0, 1.5, or 2.0% (w/v) HA after extrusion at 1.5 μL/s. Green indicates live cells; red indicates dead cells. The scale bar indicates 200 μm. (b) Experimental validation results comparing actual vs. predicted cell viability for the HUEhT-1 bioinks. Data are mean ± S.D., $n \geq 10$ for each data point.

similar wall shear stress magnitudes, aligning with previous research findings that prolonged exposure to shear stress negatively impacts the cell viability of MSCs [45].

Furthermore, cell viability after extrusion varied significantly for each cell line (Figure 11(a)). HUEhT-1 cells showed the least resistance to shear stress. HeLa cells showed some resistance to shear stress but still suffered high cell damage when exposed to high shear stress at an extended exposure time. UE7T-13 encountered a moderate decrease in cell viability at lower shear stress magnitude but showed strong resistance at higher shear stress magnitudes than HeLa cells. Meanwhile, 10T1/2 cells showed strong resistance to high shear stress even at extended cell resistance time. A previous study shows that human fibroblast cells can maintain high cell viability (> 94%) under wall shear stress around 5 kPa, although the exposure time has not been studied [22]. In this study, the 10T1/2 cells maintained around 94% cell viability at 5 kPa wall shear stress and an exposure time of 115 ms (Figure 11(b)).

The distinct responses of different cell lines to shear stress and exposure time raise questions about the underlying mechanisms. At the moment, the detailed mechanism of how each cell line used in this study showed different susceptibility to the magnitude of shear stress and exposure time to the shear stress is unknown. However, there is a possibility that this might be mediated by the distinct characteristics of these cells. Endothelial cells are known to be susceptible to a high magnitude of shear stress [58]. Cancer cells are known

Table 3. Cell viability prediction assessment for composite ALG-HA bioink containing HUEhT-1 cells.

Ink type	Extrusion rate (μL/s)	Wall shear stress (kPa)	Exposure time (ms)	Observed cell viability (%)	Predicted cell viability (%)	Prediction MAE (%)
ALG4-HA1	1.0	1.14	570	94.99 ± 3.14	88.39	6.60
	1.5	1.56	380	93.68 ± 2.76	89.62	4.06
	2.0	1.78	290	90.71 ± 4.19	87.62	3.09
	3.0	1.99	190	88.25 ± 2.85	86.47	1.78
ALG4-HA1.5	1.0	2.09	570	74.85 ± 4.40	66.72	8.13
	1.5	2.27	380	75.00 ± 3.20	72.56	2.44
	2.0	2.41	290	73.68 ± 2.98	75.00	1.32
	3.0	2.62	190	76.69 ± 3.53	78.14	1.45
ALG4-HA2	1.0	2.99	570	32.24 ± 3.35	25.43	6.81
	1.5	3.26	380	29.36 ± 3.24	30.81	1.45
	2.0	3.46	290	38.85 ± 4.42	35.93	2.92
	3.0	3.88	190	33.39 ± 2.21	34.35	0.96

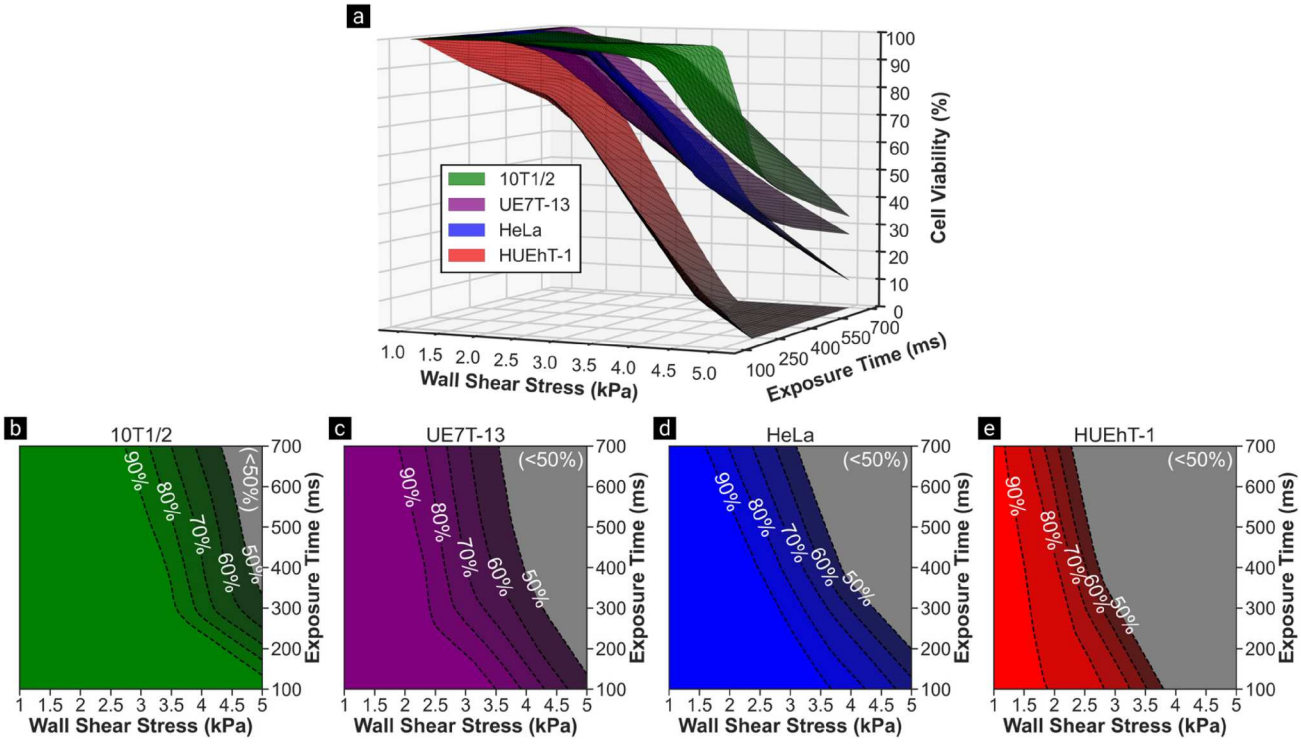

Figure 11. (a) Overlaid cell viability surface plot for 10T1/2, UE7T-13, HeLa, and HUEhT-1 cells. (b-e) Wall shear stress and exposure time contour plot marked with threshold lines for maintaining 90% to 50% cell viability for each cell line.

for their rapid adaptability to their surrounding environment [59]. However, the extrusion process happens in hundreds of milliseconds and does not allow them to adapt dynamically. On the other hand, fibroblast cells' cytoskeleton provides robust structural integrity, allowing them to withstand moderate mechanical stress [60]. The cytoskeleton's ability to withstand mechanical stress is a crucial determinant of cell rheological behaviour [61]. The cell viability results in this research suggest that fibroblast cells have stronger structural integrity than cervical cancer, mesenchymal stem, and endothelial cells.

While these cell-type-specific responses provide valuable insights, the complexity of bioink formulations adds another layer of consideration in predicting cell viability. To further validate the model's applicability to more complex formulations, experimental validation using composite ALG-HA bioinks was conducted (Figure 10). ALG4-HA1 bioink containing HUEhT-1 cells resulted in higher overall cell viability compared to 4.0% (w/v) ALG bioink, suggesting that the HA can potentially improve the shear-thinning properties of the bioink. As the HA concentration increased, the cell viability of HUEhT-1 cells dropped dramatically. These results highlighted the importance of fine-tuning the bioink formulation for optimal cell viability. Meanwhile, some deviations between observed and predicted values were noted (Table 3). These deviations suggest that while the model captures the general behaviour of composite bioinks, it may require additional fine-tuning for optimal accuracy with specific ink formulations. The addition of HA to ALG introduces new rheological complexities that may not be fully captured by the current model parameters; factors such as changes in ink homogeneity or alterations in cell–material interactions could contribute to these discrepancies. To improve model accuracy and applicability, expanding the training dataset is crucial. Incorporating a wider range of bioink formulations could enhance the model's ability to generalise across different ink compositions. Nonetheless, the models are rapidly adaptable to not only single but also composite bioinks.

Considering the ink rheological stability and cell viability findings, achieving an optimised bioprinting workflow requires a balance between these two factors. In particular, ALG inks showed enhanced rheological stability at higher concentrations (Figure 5(b)). However, despite the improved rheological stability, HUEhT-1 and HeLa cells suffered a high reduction in cell viability at these concentrations, making them unsuitable for bioprinting. However, at 6.0% (w/v) ink concentration, the viability of 10T1/2 cells could be as high as 96.1 ± 2.6% when the extrusion rate was at 3.0 µL/s (Figure 8(b)). This suggests that ALG bioink containing 10T1/2 cells can simultaneously achieve high cell viability and ink rheological stability. For UE7T-13 cells, cell

viability could reach 90.28 ± 1.78% at 3.0 µL/s at 5.0% (w/v) (Figure 8(c)). For HeLa cells, 5.0% (w/v) is preferable as the cell viability was above 94.7 ± 1.5% at an extrusion rate from 1.5 to 3.0 µL/s (Figure 8(d)). For HUEhT-1 cells, a concentration below 4.5% (w/v) ink is suitable as the cell viability was above 80.9 ± 3.0% at an extrusion rate from 1.0 to 3.0 µL/s; the cell viability could be maintained at 90.2 ± 2.9% when extruding at 1.5 µL/s with 4.0% (w/v) ink (Figure 8(e)).

In summary, this study's numerical simulations and machine-learning models offer a robust framework for predicting and optimising cell viability based on wall shear stress and exposure time. By integrating experimental data, numerical simulations, and machine learning models, a comprehensive approach to enhancing the bioprinting process is established. This framework can be readily adapted to other bioinks and cell types, facilitating the development of more effective bioprinting protocols. Although the current study provides insights on cell-type-specific response to shear stress, it focuses primarily on immediate as-extruded cell viability. Future research should explore the long-term effects of shear stress on cell proliferation and function, as cells experiencing high shear stress may undergo delayed apoptosis [62]. Moreover, the framework does not currently account for scaffold design parameters such as pore size and porosity. These factors play a crucial role in cell proliferation and overall tissue engineering outcomes, as demonstrated in works by Cheah et al. [63,64] and Naing et al. [65]. Future iterations of the predictive models should aim to integrate scaffold design parameters, combining shear stress and exposure time analysis with computational models of scaffold geometry.

5. Conclusion

This study comprehensively investigates as-extruded cell viability for diverse cell lines, wall shear stress, and exposure time in extrusion-based 3D bioprinting. The SVR models developed in this study accurately predicted ALG inks' Cross Power Law parameters based on their concentrations and temperatures. The SVR-predicted parameters in CFD simulations allowed accurate and rapid characterisation of the ink flow behaviour and shear stress distribution inside the cylindrical needle printhead. Training the MLP regressors using the simulation and experimental cell viability data resulted in an accurate prediction and optimisation of as-extruded cell viability based on wall shear stress and exposure time for each cell line. These results highlighted the critical role of shear stress magnitude and exposure time in determining as-extruded cell viability, with vascular endothelial cells being the most sensitive, followed by cervical cancer, mesenchymal stem, and embryonic fibroblast cells. The framework demonstrates a robust and generalisable approach that is rapidly adaptable to various bioinks and cell types, accelerating the bioink optimisation process. Experimental validation further confirmed the framework's effectiveness and applicability in improving the precision of bioink formulations and extrusion parameters to achieve optimal cell viability. Furthermore, this study highlights the critical balance between rheological stability and cell viability, with higher ink concentrations enhancing stability but increasing shear stress magnitude. In conclusion, this study establishes a framework for researchers to rapidly predict and optimise as-extruded cell viability for various cell types in extrusion-based 3D bioprinting and advances the design and optimisation of bioinks for tissue engineering applications.

Acknowledgment

The graphical abstract was created with BioRender.com. Colin Zhang acknowledges the support received from the Japanese Ministry of Education, Culture, Sports, Science and Technology. Wildan Mubarok acknowledges the support of the Japan Society for the Promotion of Science (JSPS) Postdoctoral Fellowship in Japan.

Disclosure statement

No potential conflict of interest was reported by the author(s).

Funding

This study was funded by the Adaptable and Seamless Technology Transfer Program through Target-driven R&D (A-STEP) from the Japan Science and Technology Agency (JST) [grant number JPMJTR234C].

CRediT author statement

Colin Zhang: Conceptualisation, Methodology, Software, Validation, Formal analysis, Investigation, Data Curation, Writing – Original Draft, Writing – Review & Editing, Visualisation. **Kelum Chamara Manoj Lakmal Elvitigala:** Validation, Investigation, Data Curation, Writing – Review & Editing. **Wildan Mubarok:** Conceptualisation, Methodology, Writing – Review & Editing. **Yasunori Okano:** Methodology, Resources, Writing – Review & Editing. **Shinji Sakai:** Conceptualisation, Methodology, Resources, Writing – Review & Editing, Supervision.

Data availability statement

The data supporting this study's findings are available from the corresponding author upon reasonable request.

Code availability statement

The scripts used for data analysis, machine learning models, and numerical simulations in this study are available on GitHub at: https://github.com/KORINZ/in-silico-bioink-viability-prediction.

ORCID

Colin Zhang http://orcid.org/0009-0009-2411-9640
Kelum Chamara Manoj Lakmal Elvitigala http://orcid.org/0000-0002-9649-0635
Wildan Mubarok http://orcid.org/0000-0003-2545-1206
Yasunori Okano http://orcid.org/0000-0003-3710-2492
Shinji Sakai http://orcid.org/0000-0002-1041-4798

References

[1] Landers R, Hübner U, Schmelzeisen R, et al. Rapid prototyping of scaffolds derived from thermoreversible hydrogels and tailored for applications in tissue engineering. Biomaterials. 2002;23(23):4437–4447. doi:10.1016/S0142-9612(02)00139-4
[2] Groll J, Boland T, Blunk T, et al. Biofabrication: reappraising the definition of an evolving field. Biofabrication. 2016;8(1):013001. doi:10.1088/1758-5090/8/1/013001
[3] Groll J, Burdick JA, Cho D-W, et al. A definition of bioinks and their distinction from biomaterial inks. Biofabrication. 2018;11(1):013001. doi:10.1088/1758-5090/aaec52
[4] Mandrycky C, Wang Z, Kim K, et al. 3D bioprinting for engineering complex tissues. Biotechnol Adv. 2016;34(4):422–434. doi:10.1016/j.biotechadv.2015.12.011
[5] Ozbolat IT, Hospodiuk M. Current advances and future perspectives in extrusion-based bioprinting. Biomaterials. 2016;76:321–343. doi:10.1016/j.biomaterials.2015.10.076
[6] Jiang T, Munguia-Lopez JG, Flores-Torres S, et al. Extrusion bioprinting of soft materials: An emerging technique for biological model fabrication. Appl Phys Rev. 2019;6(1):011310. doi:10.1063/1.5059393
[7] Cui X, Li J, Hartanto Y, et al. Advances in extrusion 3D bioprinting: A focus on multicomponent hydrogel-based bioinks. Adv Healthc Mater. 2020;9(15):1901648. doi:10.1002/adhm.201901648
[8] Zhang YS, Haghiashtiani G, Hübscher T, et al. 3D extrusion bioprinting. Nat Rev Methods Primer. 2021;1(1):1–20. doi:10.1038/s43586-021-00073-8
[9] Li X, Zheng F, Wang X, et al. Biomaterial inks for extrusion-based 3D bioprinting: property, classification, modification, and selection. Int J Bioprinting. 2023;9(2):649–649. doi:10.18063/ijb.v9i2.649
[10] Cooke ME, Rosenzweig DH. The rheology of direct and suspended extrusion bioprinting. APL Bioeng. 2021;5(1):011502. doi:10.1063/5.0031475
[11] Hölzl K, Lin S, Tytgat L, et al. Bioink properties before, during and after 3D bioprinting. Biofabrication. 2016;8(3):032002. doi:10.1088/1758-5090/8/3/032002
[12] Highley CB, Rodell CB, Burdick JA. Direct 3D printing of shear-thinning hydrogels into self-healing hydrogels. Adv Mater. 2015;27(34):5075–5079. doi:10.1002/adma.201501234
[13] Kitana W, Levario-Diaz V, Cavalcanti-Adam EA, et al. Biofabrication of composite bioink-nanofiber constructs: effect of rheological properties of bioinks on 3D (bio)-printing and cells interaction with aligned touch spun nanofibers. Adv Healthc Mater. 2024;13(6):2303343. doi:10.1002/adhm.202303343
[14] Gao C, Tang L, Qu H, et al. A small-molecule polycationic crosslinker boosts alginate-based bioinks for extrusion bioprinting. Adv Funct Mater. 2024;34(9):2310369. doi:10.1002/adfm.202310369
[15] Markstedt K, Mantas A, Tournier I, et al. 3D bioprinting human chondrocytes with nanocellulose–alginate bioink for cartilage tissue engineering applications. Biomacromolecules. 2015;16(5):1489–1496. doi:10.1021/acs.biomac.5b00188
[16] Ning L, Betancourt N, Schreyer DJ, et al. Characterization of cell damage and proliferative ability during and after bioprinting. ACS Biomater Sci Eng. 2018;4(11):3906–3918. doi:10.1021/acsbiomaterials.8b00714
[17] Emmermacher J, Spura D, Cziommer J, et al. Engineering considerations on extrusion-based bioprinting: interactions of material behavior, mechanical forces and cells in the printing needle. Biofabrication. 2020;12(2):025022. doi:10.1088/1758-5090/ab7553
[18] Navara AM, Xu Y, Perez MR, et al. Aspects of a suspended bioprinting system affect cell viability and support bath properties. Tissue Eng Part A. 2024;30(11-12):256–269. doi:10.1089/ten.tea.2023.0097
[19] Han S, Kim CM, Jin S, et al. Study of the process-induced cell damage in forced extrusion bioprinting. Biofabrication. 2021;13(3):035048. doi:10.1088/1758-5090/ac0415
[20] Xu H-Q, Liu J-C, Zhang Z-Y, et al. A review on cell damage, viability, and functionality during 3D bioprinting. Mil Med Res. 2022;9(1):70. doi:10.1186/s40779-022-00429-5
[21] Xin S, Deo KA, Dai J, et al. Generalizing hydrogel microparticles into a new class of bioinks for extrusion bioprinting. Sci Adv. 2021;7(42):eabk3087. doi:10.1126/sciadv.abk3087
[22] Blaeser A, Duarte Campos DF, Puster U, et al. Controlling shear stress in 3D bioprinting is a key factor to balance printing resolution and stem cell integrity. Adv Healthc Mater. 2016;5(3):326–333. doi:10.1002/adhm.201500677
[23] Rossi A, Pescara T, Gambelli AM, et al. Biomaterials for extrusion-based bioprinting and biomedical applications. Front Bioeng Biotechnol. 2024;12; doi:10.3389/fbioe.2024.1393641
[24] Zhang Y, O'Mahony A, He Y, et al. Hydrodynamic shear stress' impact on mammalian cell properties and its applications in 3D bioprinting. Biofabrication. 2024;16(2):022003. doi:10.1088/1758-5090/ad22ee
[25] Jia J, Richards DJ, Pollard S, et al. Engineering alginate as bioink for bioprinting. Acta Biomater. 2014;10(10):4323–4331. doi:10.1016/j.actbio.2014.06.034
[26] Zhao F, Cheng J, Sun M, et al. Digestion degree is a key factor to regulate the printability of pure tendon decellularized extracellular matrix bio-ink in extrusion-based 3D cell printing. Biofabrication. 2020;12(4):045011. doi:10.1088/1758-5090/aba411
[27] Hinton TJ, Jallerat Q, Palchesko RN, et al. Three-Dimensional printing of complex biological structures by freeform reversible embedding of suspended hydrogels. Sci Adv. 2015;1(9):e1500758. doi:10.1126/sciadv.1500758

[28] Li H, Tan YJ, Kiran R, et al. Submerged and non-submerged 3D bioprinting approaches for the fabrication of complex structures with the hydrogel pair GelMA and alginate/methylcellulose. Addit Manuf. 2021;37:101640. doi:10.1016/j.addma.2020.101640
[29] Zhao Y, Li Y, Mao S, et al. The influence of printing parameters on cell survival rate and printability in microextrusion-based 3D cell printing technology. Biofabrication. 2015;7(4):045002. doi:10.1088/1758-5090/7/4/045002
[30] He Y, Yang F, Zhao H, et al. Research on the printability of hydrogels in 3D bioprinting. Sci Rep. 2016;6(1):29977. doi:10.1038/srep29977
[31] Li H, Liu S, Li L. Rheological study on 3D printability of alginate hydrogel and effect of graphene oxide. Int J Bioprinting. 2016;2 (2):54–66. doi:10.18063/IJB.2016.02.007
[32] Ouyang L, Yao R, Zhao Y, et al. Effect of bioink properties on printability and cell viability for 3D bioplotting of embryonic stem cells. Biofabrication. 2016;8(3):035020. doi:10.1088/1758-5090/8/3/035020
[33] Chand R, Muhire BS, Vijayavenkataraman S. Computational fluid dynamics assessment of the effect of bioprinting parameters in extrusion bioprinting. Int J Bioprinting. 2022;8(2):545. doi:10.18063/ijb.v8i2.545
[34] Ates G, Bartolo P. Computational fluid dynamics for the optimization of internal bioprinting parameters and mixing conditions. Int J Bioprinting. 2023;9(6):0219. doi:10.36922/ijb.0219
[35] Sánchez-Sánchez R, Rodríguez-Rego JM, Macías-García A, et al. Relationship between shear-thinning rheological properties of bioinks and bioprinting parameters. Int J Bioprinting. 2023;9(2):687. doi:10.18063/ijb.687
[36] Hauswirth SC, Bowers CA, Fowler CP, et al. Modeling cross model non-Newtonian fluid flow in porous media. J Contam Hydrol. 2020;235:103708. doi:10.1016/j.jconhyd.2020.103708
[37] Mohammadrezaei D, Podina L, Silva JD, et al. Cell viability prediction and optimization in extrusion-based bioprinting via neural network-based Bayesian optimization models. Biofabrication. 2024;16(2):025016. doi:10.1088/1758-5090/ad17cf
[38] Lee S, Sani ES, Spencer AR, et al. Human-Recombinant-Elastin-Based bioinks for 3D bioprinting of vascularized soft tissues. Adv Mater. 2020;32(45):2003915. doi:10.1002/adma.202003915
[39] Gospodinova A, Nankov V, Tomov S, et al. Extrusion bioprinting of hydroxyethylcellulose-based bioink for cervical tumor model. Carbohydr Polym. 2021;260:117793. doi:10.1016/j.carbpol.2021.117793
[40] Duarte Campos DF, Blaeser A, Buellesbach K, et al. Bioprinting organotypic hydrogels with improved mesenchymal stem cell remodeling and mineralization properties for bone tissue engineering. Adv Healthc Mater. 2016;5(11):1336–1345. doi:10.1002/adhm.201501033
[41] Liu P, Li Q, Yang Q, et al. Evaluation of the effect of 3D-bioprinted gingival fibroblast-encapsulated ADM scaffolds on keratinized gingival augmentation. J Periodontal Res. 2023;58(3):564–574. doi:10.1111/jre.13126
[42] Zhang F, O'Donnell LJ. Chapter 7 - support vector regression. In: Mechelli A, Vieira S, editors. *Machine learning*. CF: Academic Press; 2020. p. 123–140. doi:10.1016/B978-0-12-815739-8.00007-9
[43] Agirre-Basurko E, Ibarra-Berastegi G, Madariaga I. Regression and multilayer perceptron-based models to forecast hourly O3 and NO2 levels in the Bilbao area. Environ Model Softw. 2006;21(4):430–446. doi:10.1016/j.envsoft.2004.07.008
[44] Baptista ML, Goebel K, Henriques EM. Relation between prognostics predictor evaluation metrics and local interpretability SHAP values. Artif Intell. 2022;306:103667. doi:10.1016/j.artint.2022.103667
[45] Paxton N, Smolan W, Böck T, et al. Proposal to assess printability of bioinks for extrusion-based bioprinting and evaluation of rheological properties governing bioprintability. Biofabrication. 2017;9(4):044107. doi:10.1088/1758-5090/aa8dd8
[46] Gallagher MT, Wain RAJ, Dari S, et al. Non-Identifiability of parameters for a class of shear-thinning rheological models, with implications for haematological fluid dynamics. J Biomech. 2019;85:230–238. doi:10.1016/j.jbiomech.2019.01.036
[47] Cross MM. Rheology of non-Newtonian fluids: A new flow equation for pseudoplastic systems. J Colloid Sci. 1965;20(5):417–437. doi:10.1016/0095-8522(65)90022-X
[48] Gastone F, Tosco T, Sethi R. Green stabilization of microscale iron particles using guar gum: bulk rheology, sedimentation rate and enzymatic degradation. J Colloid Interface Sci. 2014;421:33–43. doi:10.1016/j.jcis.2014.01.021
[49] Khan M, Manzur M, ur Rahman M. On axisymmetric flow and heat transfer of cross fluid over a radially stretching sheet. Results Phys. 2017;7:3767–3772. doi:10.1016/j.rinp.2017.08.039
[50] Ramedani Z, Omid M, Keyhani A, et al. Potential of radial basis function based support vector regression for global solar radiation prediction. Renew Sustain Energy Rev. 2014;39:1005–1011. doi:10.1016/j.rser.2014.07.108
[51] Greenshields C, Weller H. *Notes on computational fluid dynamics: general principles*. Reading: CFD Direct Ltd; 2022.
[52] Weller HG, Tabor G, Jasak H, et al. A tensorial approach to computational continuum mechanics using object-oriented techniques. Comput Phys. 1998;12(6):620–631. doi:10.1063/1.168744
[53] Kuhn M, Johnson K. Factors that Can affect model performance. In: Kuhn M, Johnson K, editors. *Applied predictive modeling*. New York, NY: Springer; 2013. p. 521–546. doi:10.1007/978-1-4614-6849-3_20.
[54] Kingma DP, Ba J. Adam: a method for stochastic optimization. arXiv January 29, 2017. doi:10.48550/arXiv.1412.6980.
[55] Webb B, Doyle BJ. Parameter optimization for 3D bioprinting of hydrogels. Bioprinting. 2017;8:8–12. doi:10.1016/j.bprint.2017.09.001
[56] Wu Q, Therriault D, Heuzey M-C. Processing and properties of chitosan inks for 3D printing of hydrogel microstructures. ACS Biomater Sci Eng. 2018;4(7):2643–2652. doi:10.1021/acsbiomaterials.8b00415
[57] Kiyotake EA, Douglas AW, Thomas EE, et al. Development and quantitative characterization of the precursor rheology of hyaluronic acid hydrogels for bioprinting. Acta

Biomater. 2019;95:176–187. doi:10.1016/j.actbio.2019.01.041

[58] Russo TA, Banuth AMM, Nader HB, et al. Altered shear stress on endothelial cells leads to remodeling of extracellular matrix and induction of angiogenesis. PLoS One. 2020;15(11):e0241040. doi:10.1371/journal.pone.0241040

[59] Cairns RA, Harris IS, Mak TW. Regulation of cancer cell metabolism. Nat Rev Cancer. 2011;11(2):85–95. doi:10.1038/nrc2981

[60] Heidemann SR, Kaech S, Buxbaum RE, et al. Direct observations of the mechanical behaviors of the cytoskeleton in living fibroblasts. J Cell Biol. 1999;145(1):109–122. doi:10.1083/jcb.145.1.109

[61] Rosenblatt N, Hu S, Chen J, et al. Distending stress of the cytoskeleton is a key determinant of cell rheological behavior. Biochem Biophys Res Commun. 2004;321(3):617–622. doi:10.1016/j.bbrc.2004.07.011

[62] Bartling B, Tostlebe H, Darmer D, et al. Shear stress-dependent expression of apoptosis-regulating genes in endothelial cells. Biochem Biophys Res Commun. 2000;278(3):740–746. doi:10.1006/bbrc.2000.3873

[63] Cheah CM, Chua CK, Leong KF, et al. Development of a tissue engineering scaffold structure library for rapid prototyping. part 1: investigation and classification. Int J Adv Manuf Technol. 2003;21(4):291–301. doi:10.1007/s001700300034

[64] Cheah CM, Chua CK, Leong KF, et al. Development of a tissue engineering scaffold structure library for rapid prototyping. part 2: parametric library and assembly program. Int J Adv Manuf Technol. 2003;21(4):302–312. doi:10.1007/s001700300035

[65] Naing MW, Chua CK, Leong KF, et al. Fabrication of customised scaffolds using computer-aided design and rapid prototyping techniques. Rapid Prototyp J. 2005;11(4):249–259. doi:10.1108/13552540510612938

Appendix

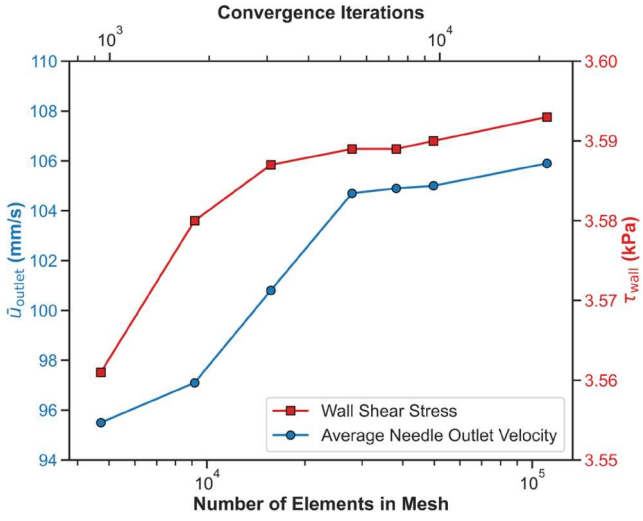

Figure A1. Mesh dependence test for the 27-gauge cylindrical needle simulation mesh with ALG 5.5% (w/v) ink at 25 °C and an extrusion rate of 3.0 µL/s.

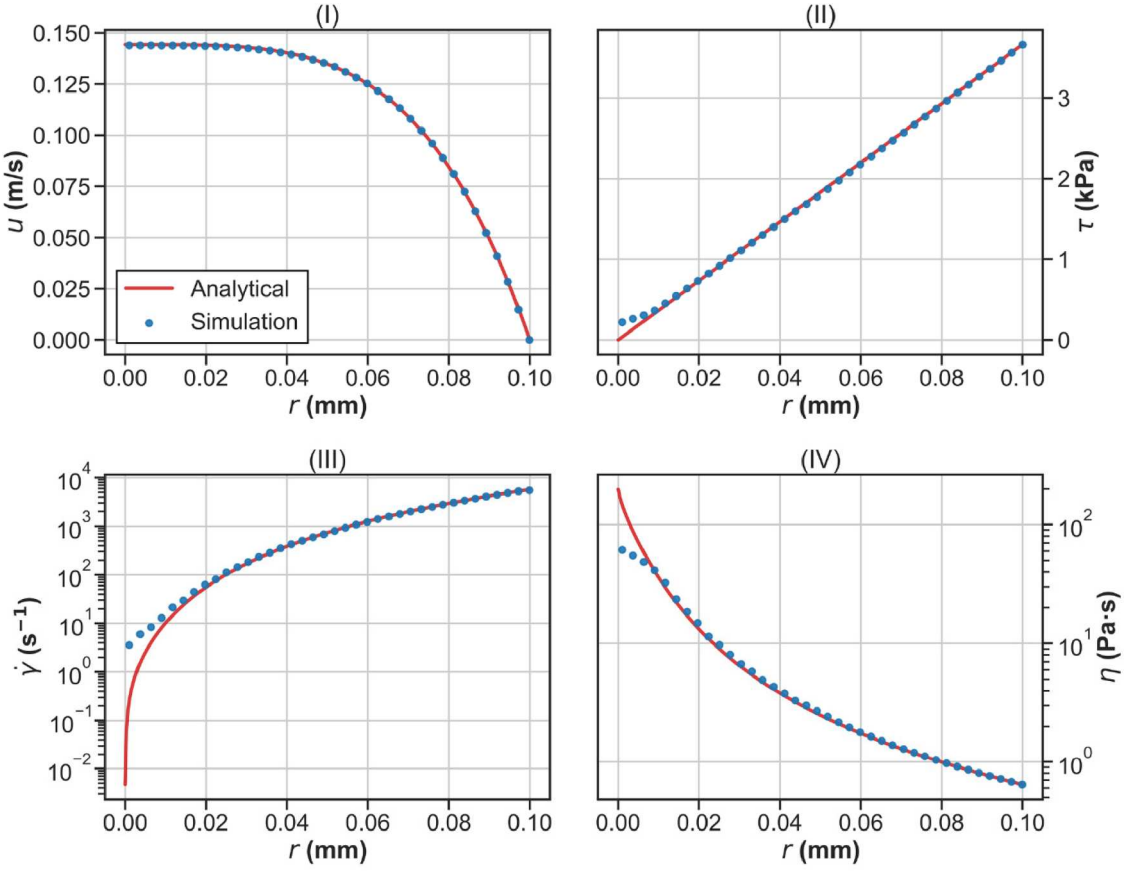

Figure A2. Comparison between analytical and simulation results for ALG ink at 5.5% (w/v) at 25 °C with a flow rate of 3.0 µL/s at the needle outlet (radial distance). (I) radial velocity; (II) shear stress; (III) shear rate; (IV) apparent viscosity.

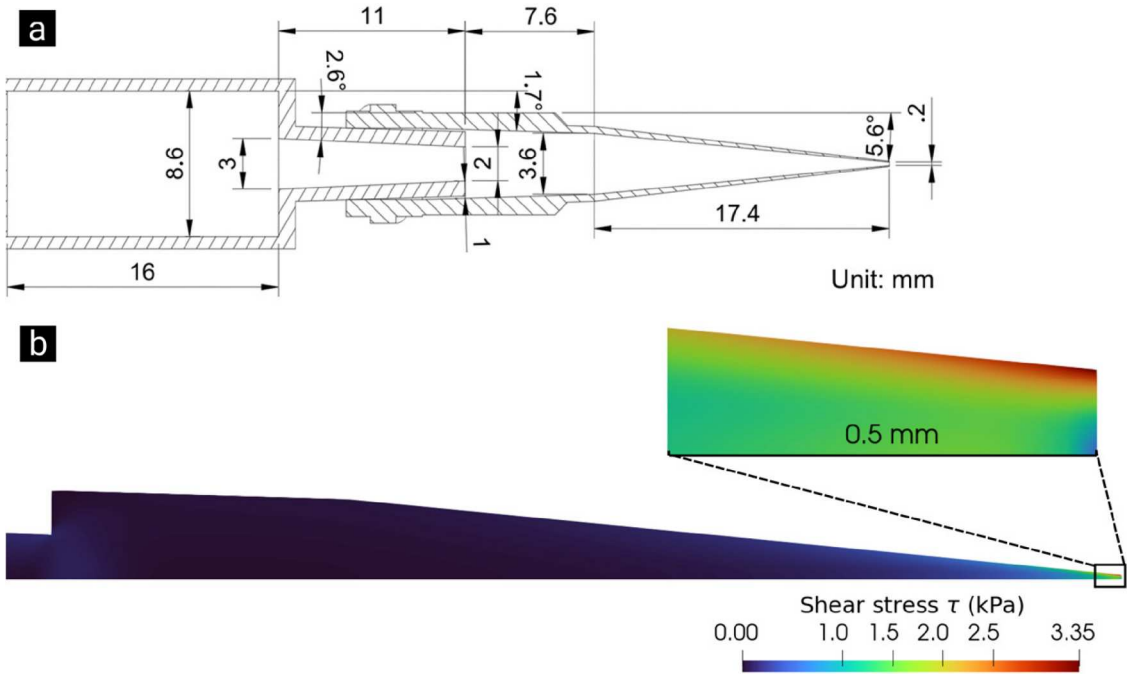

Figure A3. (a) Engineering drawing of the syringe and tapered printhead. (b) CFD simulation result of shear stress distribution for 5.0% (w/v) ALG ink at 22.5 °C with an extrusion rate of 1.5 µL/s inside the tapered 27-gauge nozzle printhead. Numerical simulations of a 27-gauge tapered nozzle printhead (TPND-27G-U; Musashi Engineering, Inc., Tokyo, Japan) were carried out based on Section 2.7.

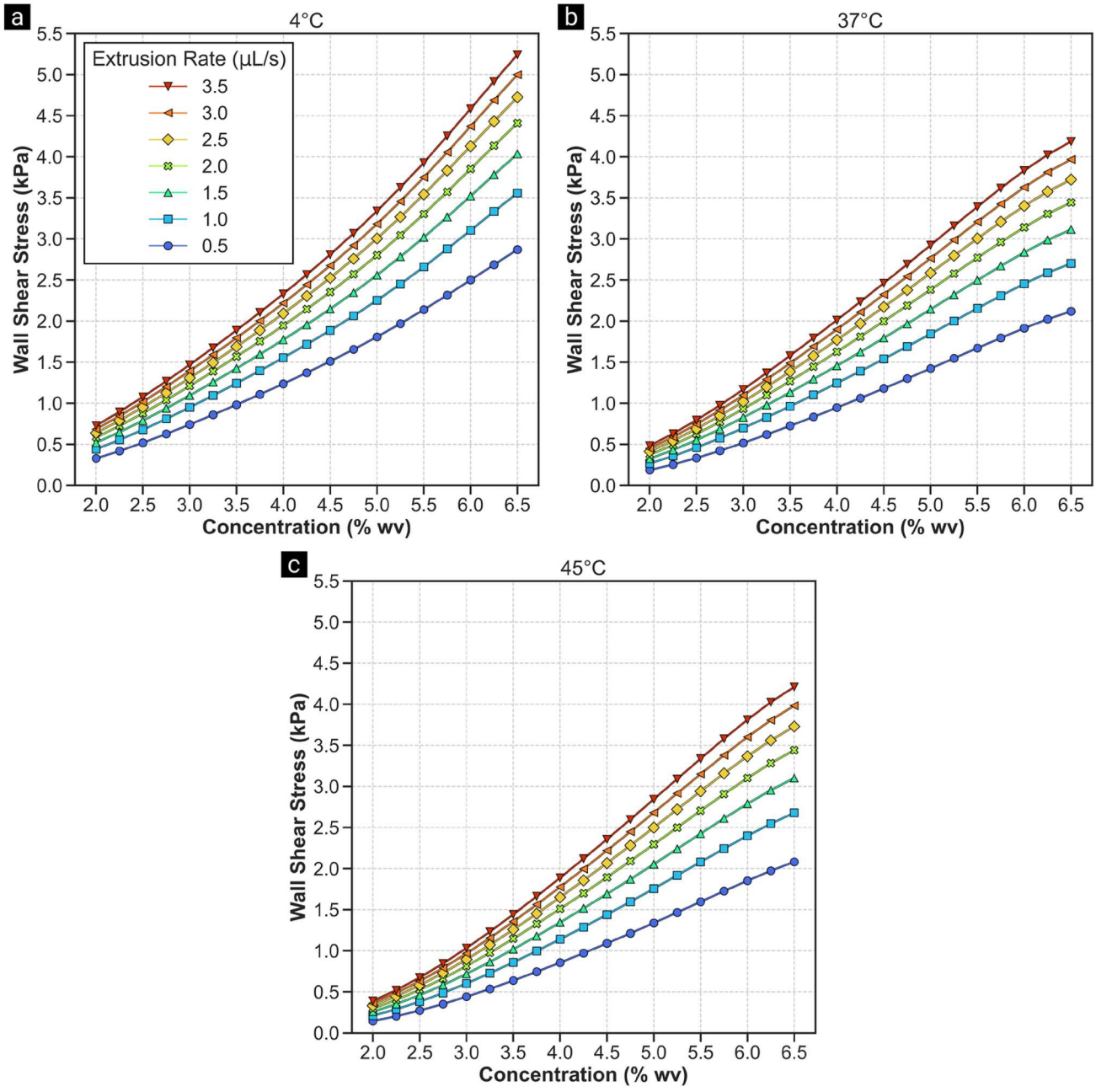

Figure A4. ALG ink concentration vs. wall shear stress with extrusion rates of 0.5–3.5 μL/s at (a) 4 °C, (b) 37 °C, and (c) 45 °C.

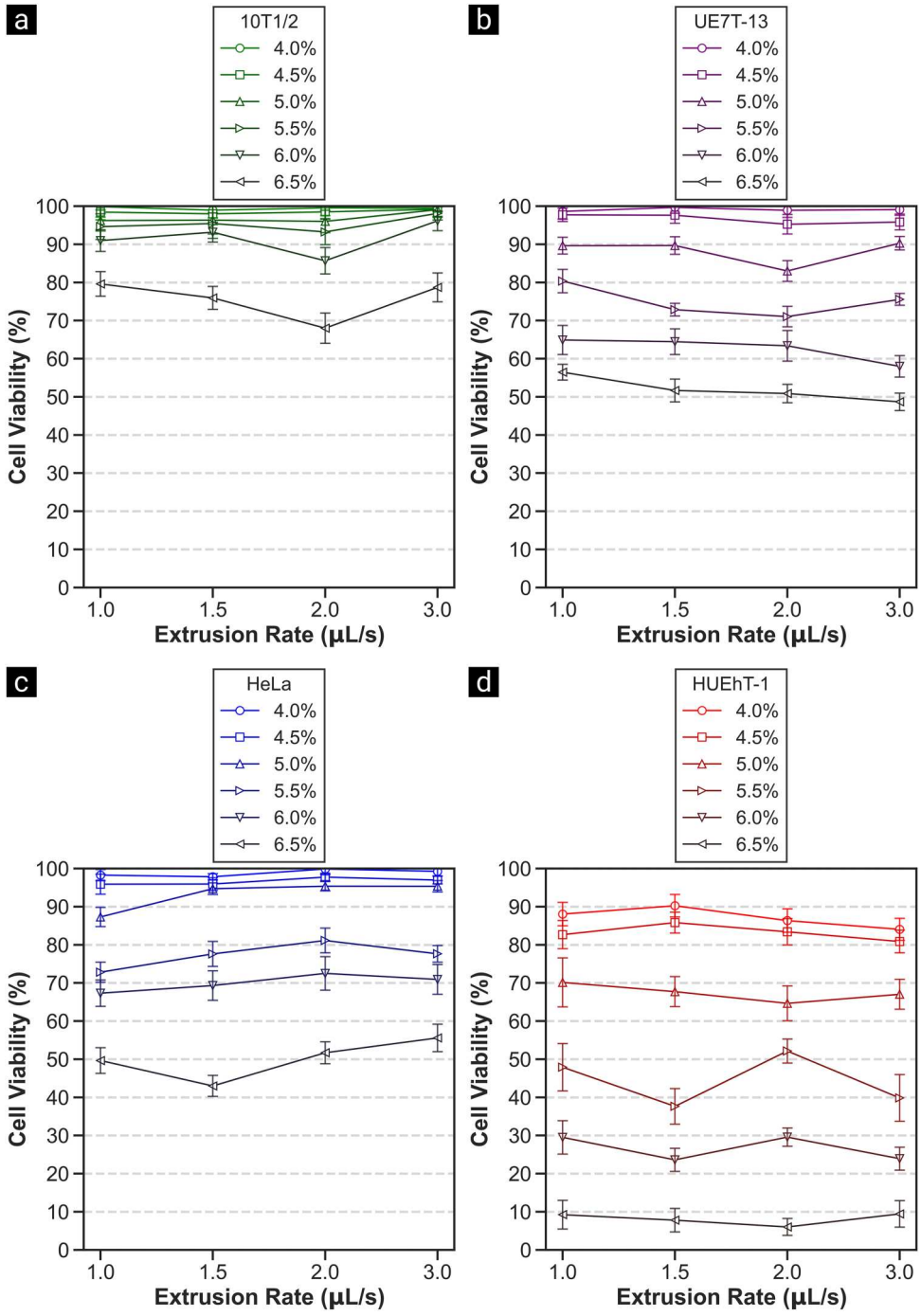

Figure A5. Cell viability vs. extrusion rate line plots for ALG inks containing (a) 10T1/2, (b) UE7T-13, (c) HeLa, and (d) HUEhT-1 cells. Data are mean ± S.D., $n \geq 8$ for each data point.

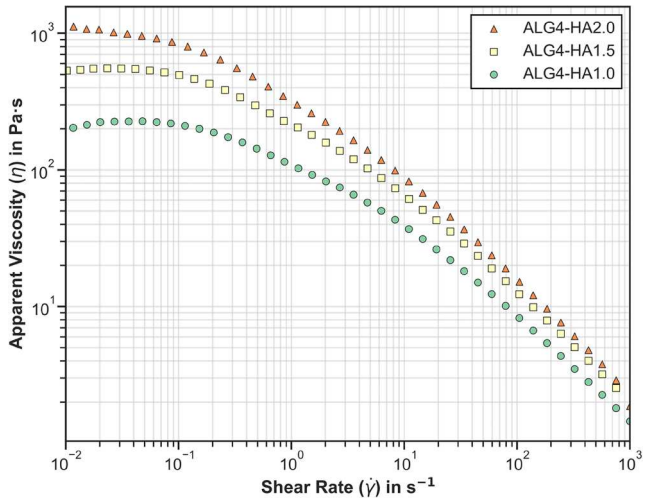

Figure A6. Apparent viscosity vs. shear rate curves for ALG and HA composite polymer inks at 22.5 °C.

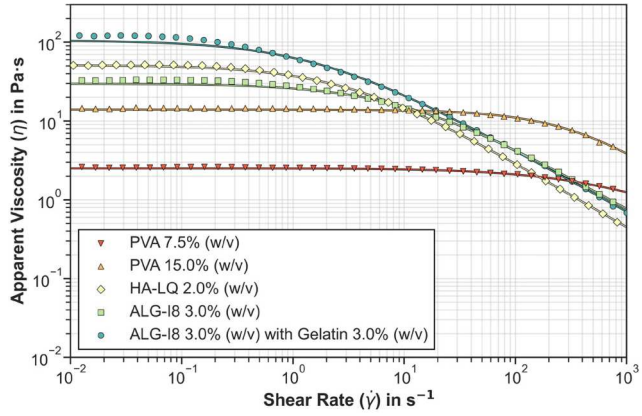

Figure A7. Apparent viscosity vs. shear rate curves for PVA, HA, and ALG-I8 polymer inks. Solid lines represent Cross Power Law fittings, while symbols represent experimental data. PVA (molecular weight ≈ 146–186 kDa; 99+% hydrolysed) and gelatin (from bovine skin; type B; gel strength ~ 225 g bloom) were sourced from Sigma-Aldrich (St. Louis, MO, USA). High-molecular-weight sodium alginate (ALG-I8; mannuronic acid/guluronic acid ratio ≈ 1.0; molecular weight ≈ 3,200 kDa) was sourced from KIMICA Corporation (Tokyo, Japan).